Author/s:
Santavanond, JP;Atkin-Smith, GK;González, IL;Carol, JR;Jiang, L;Hodge, AL;Ozkocak, DC;Zhao, K;Gray, DHD;Herold, MJ;Kueh, AJ;Ryan, GF;Tixeira, R;Olson, MF;Hulett, MD;Baxter, AA;Poon, IKH;Hoijman, E

Title:
Resident phagocytes promote non–cell-autonomous fragmentation of apoptotic cells

Date:
2025-12-17

Citation:
Santavanond, J. P., Atkin-Smith, G. K., González, I. L., Carol, J. R., Jiang, L., Hodge, A. L., Ozkocak, D. C., Zhao, K., Gray, D. H. D., Herold, M. J., Kueh, A. J., Ryan, G. F., Tixeira, R., Olson, M. F., Hulett, M. D., Baxter, A. A., Poon, I. K. H. & Hoijman, E. (2025). Resident phagocytes promote non–cell-autonomous fragmentation of apoptotic cells. Science Advances, 11 (51), pp.1-15. https://doi.org/10.1126/sciadv.adz5264.

Persistent Link:
https://hdl.handle.net/11343/368101

CELL BIOLOGY

Resident phagocytes promote non–cell-autonomous fragmentation of apoptotic cells

Jascinta P. Santavanond[1,2]†, Georgia K. Atkin-Smith[1,2,3,4]†, Irene Lozano-González[5,6], Joan Roncero-Carol[6], Lanzhou Jiang[1,2], Amy L. Hodge[1,2], Dilara C. Ozkocak[1,2], Kelin Zhao[3,4], Daniel H. D. Gray[3,4], Marco J. Herold[3,4,7,8], Andrew J. Kueh[3,4], Gemma F. Ryan[1,2], Rochelle Tixeira[9,10], Michael F. Olson[11], Mark D. Hulett[1,2], Amy A. Baxter[1,2], Ivan K. H. Poon[1,2]*, Esteban Hoijman[5,6]*

Phagocytosis of apoptotic cells maintains tissue homeostasis and regulates inflammation. A proposed facilitator of apoptotic cell clearance is the fragmentation of these cells into apoptotic bodies (ApoBDs) through cell-autonomous processes involving caspases and cytoskeletal rearrangement. Although this fragmentation process is considered a hallmark of apoptosis, its progression in tissue environments remains underexplored. Here, we examine the in vivo apoptotic dynamics of mouse thymocytes and pluripotent cells from zebrafish embryos. We show that the in vivo biogenesis of ApoBDs is independent of known cell-intrinsic regulators. Instead, fragmentation depends on actin-rich protrusions from neighboring resident phagocytes, which mechanically compress apoptotic cells to break them into smaller particles. Four-dimensional in vivo tracking of apoptotic cells reveals that both phagocyte-mediated fragmentation and phagocytosis are size sensitive, indicating that apoptotic size reduction mediated by phagocytes enhances their own clearance abilities. This non–cell-autonomous fragmentation ensures rapid apoptotic cell clearance, crucial for maintaining tissue homeostasis in physiological settings.

INTRODUCTION

Apoptosis is often considered as an immunologically silent form of cell death that allows dying cells to be removed by phagocytes without triggering inflammation. Therefore, it plays a crucial role in physiological states such as morphogenesis and tissue homeostasis, and its dysregulation leads to inflammatory diseases, cancer, and neurodegeneration (*1*–*5*). It is well described that apoptotic cells use molecular "find-me" and "eat-me" signals to mediate their clearance by phagocytes (*6*–*14*). However, despite efficient uptake of apoptotic cells by phagocytes involving various mechanical processes mediated by cytoskeletal rearrangement (*15*–*18*), the biophysical constraints that regulate this process are less well understood.

Morphologically, apoptosis is characterized by a controlled cell disassembly process involving plasma membrane blebbing, formation of thin membrane protrusions (i.e., apoptopodia), followed by fragmentation into distinct membrane-bound vesicles known as apoptotic bodies (ApoBDs) (*19*–*24*). This cell-intrinsic (or cell-autonomous) fragmentation is regulated by the caspase-mediated activation of Rho-associated kinase 1 (ROCK1) and pannexin 1 (PANX1) (*19*, *21*, *23*–*25*). One proposed role of ApoBDs is that their smaller size facilitates efficient ingestion by phagocytes (*21*, *26*). This may be particularly important for settings whereby the level of cell death is high, or phagocytosis is performed predominately by nonimmune cells such as epithelial cells, which may have a more limited ability to change shape and size to engulf due to their stable junctions between them. However, only certain cultured cell types undergo fragmentation during apoptosis and in response to specific apoptotic triggers (*19*, *25*, *27*), raising questions about the universality of this process. Intriguingly, in vivo evidence of ApoBDs is widespread, appearing in many different tissues and model organisms (*18*, *28*–*33*).

Here, we explore the relevance of ApoBD formation in natural tissue contexts. We found that apoptotic cells do not require known cell-intrinsic regulators of fragmentation to generate ApoBDs in vivo in certain tissues. Instead, resident phagocytes produce protrusions that mechanically break apart apoptotic cells. This cell-extrinsic fragmentation process aids phagocytosis, highlighting the role of resident phagocytes in fragmenting apoptotic cells to facilitate clearance.

RESULTS

The in vivo environment promotes fragmentation of apoptotic thymocytes

Thymocytes experience abundant physiological cell death as part of the immune selection process during development (*34*). To study the formation of ApoBDs, first, we used a well-established model of apoptotic cell death, the dexamethasone (dex; a synthetic glucocorticoid) induction of apoptosis in the mouse thymus (*35*). We first treated thymocytes with dex in vitro and used markers of apoptosis [externalization of phosphatidylserine (PtdSer) revealed by annexin 5 (A5) staining] as well as size as an indicator of the level of apoptotic cell fragmentation (*36*). We observed that $CD4^+/CD8^+$ thymocytes rarely fragment into ApoBDs in vitro, even up to 12 hours post–dex treatment (Fig. 1, A to C, and fig. S1). In contrast, under in vivo conditions, apoptotic thymocytes readily fragmented into abundant ApoBDs

[1]Department of Biochemistry and Chemistry, La Trobe Institute for Molecular Science, La Trobe University, Melbourne, Victoria, Australia. [2]Research Centre for Extracellular Vesicles, La Trobe University, Melbourne, Victoria, Australia. [3]The Walter and Eliza Hall Institute of Medial Research, Parkville, Victoria, Australia. [4]University of Melbourne, Melbourne, Victoria, Australia. [5]Molecular Biology Institute of Barcelona, Spanish Research Council (CSIC), Barcelona, Spain. [6]Regenerative Medicine Program, Bellvitge Institute for Biomedical Research (IDIBELL), Barcelona, Spain. [7]Olivia Newton-John Cancer Research Institute, Heidelberg, Victoria, Australia. [8]School of Cancer Medicine, La Trobe University, Melbourne, Victoria, Australia. [9]Unit for Cell Clearance in Health and Disease, VIB Center for Inflammation Research, Ghent, Belgium. [10]Department of Biomedical Molecular Biology, Ghent University, Ghent, Belgium. [11]Department of Chemistry and Biology, Toronto Metropolitan University, Toronto, Ontario, Canada.
*Corresponding author. Email: i.poon@latrobe.edu.au (I.K.H.P.); ehkbmc@ibmb.csic.es (E.H.)
†These authors contributed equally to this work.

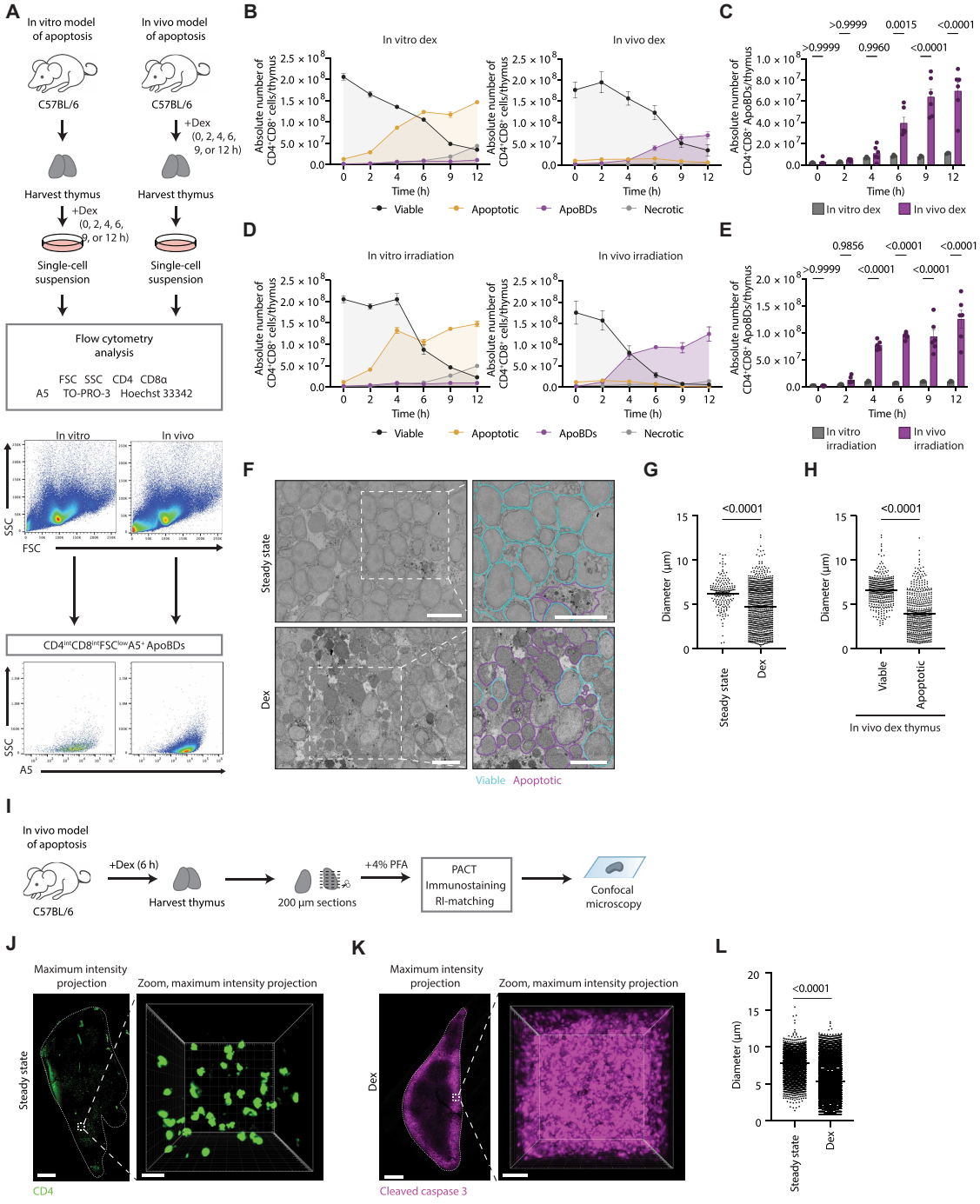

Fig. 1. The in vivo environment promotes fragmentation of apoptotic thymocytes. (**A**) Schematic of the in vitro and in vivo dex-induced apoptosis model. (**B** to **E**) Flow cytometry analysis showing absolute number of $CD4^+/CD8^+$ ApoBDs, viable, apoptotic, and necrotic cells per thymus after (B) dex (50 μM in vitro or 12.5 mg/kg in vivo) or (D) whole-body x-ray irradiation (6.8 Gy) treatment ($n = 6$). (C to E) Statistical analysis of $CD4^+/CD8^+$ ApoBDs formed in vitro and in vivo from (B) and (D). (**F**) Representative transmission electron microscopy (TEM) images of the thymus at steady state or 6 hours post–dex (12.5 mg/kg in vivo) treatment. Scale bars, 8 μm. (**G**) Quantification of the Feret diameter (μm) of cells in (F) from three regions of interest (ROIs; steady state, $n = 168$ particles; dex, $n = 905$ particles). (**H**) Quantification of the Feret diameter (μm) of viable [intact double membranes (blue); $n = 391$ particles] and apoptotic cells [heavy-metal staining and membrane ruffling (magenta); $n = 504$ particles] in the thymus 6 hours post–dex (12.5 mg/kg in vivo) treatment from three ROIs. (**I**) Thymic clearing schematic diagram using passive clearing technique (PACT) and refractive index (RI)-matching. (**J** and **K**) Representative maximum intensity projection images of cleared thymic tissue sections under steady state (J) and 6 hours post–dex (12.5 mg/kg in vivo) treatment (K), immunostained with CD4 and cleaved caspase 3 (CC3), respectively. Scale bars, (whole-organ images) 500 μm and (zoomed images) 20 and 10 μm, respectively. Data representative of ($n = 3$). (**L**) Relative particle size distribution of $CD4^+$ ($n = 8185$ particles) and $CC3^+$ ($n = 82955$ particles) particles as per (J) and (K). All error bars represent SEM. Two-way analysis of variance (ANOVA) followed by Šidák's multiple comparisons was performed for (C) and (E), and unpaired *t* test was performed for [(G), (H), and (L)] to determine the indicated *P* value. h, hours.

(Fig. 1, B and C). Consistent with our flow cytometry analysis, confocal microscopy examination of thymocyte suspensions demonstrated that the overall particle size of $A5^+$ $CD4^+/CD8^+$ thymocytes was significantly smaller when apoptosis occurred in vivo (fig. S2A), indicative of a higher level of fragmentation. Similar results were observed when thymocyte apoptosis was induced by whole-body x-ray irradiation (Fig. 1, D and E, and fig. S2B), providing evidence that the difference between in vitro and in vivo cell fragmentation is not exclusive to a specific apoptotic stimulus.

To visualize apoptotic cell fragments in situ, we performed transmission electron microscopy (TEM) analysis on thymic sections under steady-state conditions or dex treatment and analyzed cell diameter (Fig. 1F). Dex-induced apoptosis led to increased frequency of small fragments, with a mean diameter of 4.72 ± 0.16 μm (Fig. 1G). Notably, apoptotic cells (denoted by membrane ruffling and density of heavy-metal staining) were observed to be smaller in dex-treated samples when compared to neighboring viable cells (Fig. 1H). Similar results were observed in optically cleared thymic samples immunostained for CD4 and cleaved caspase 3 ($CC3^+$) (Fig. 1, I to K), whereby in vivo dex treatment resulted in the formation of $CC3^+$ particles that had a mean diameter of 5.35 ± 0.14 μm (Fig. 1L). Moreover, active caspase 3/7 were detected in both $CD4^+$ ApoBDs and apoptotic cells upon in vivo dex treatment (fig. S2C). These particles were markedly smaller than $CD4^+$ thymocytes in steady state, which had a mean diameter of 7.89 ± 0.40 μm (Fig. 1L). These results indicate that the in vivo microenvironment unexpectedly promotes the fragmentation of apoptotic thymocytes, even when clearance mechanisms are operating concurrently in vivo (*8*, *37*–*43*).

Known regulators of cell-intrinsic fragmentation are not required for the formation of thymocyte-derived ApoBDs in vivo

To explore the mechanisms underlying in vivo apoptotic cell fragmentation, we focused on known signaling pathways of cell-intrinsic fragmentation. Caspase-activated ROCK1 kinase and PANX1 membrane channels are key positive and negative regulators of apoptotic morphological processes, respectively, that are required for the biogenesis of ApoBDs (Fig. 2A) (*19*, *21*, *25*). To test the importance of these regulators in ApoBD formation in vivo, we used caspase-resistant, noncleavable ROCK1 ($ROCK1^{nc}$) and PANX1 ($PANX1^{nc}$) mice, whereby point mutations were introduced at the caspase cleavage site of each protein resulting in constitutively expressed caspase-resistant ROCK1 and PANX1 proteins (Fig. 2B and fig. S3, A and B) (*44*–*47*). As expected, in vitro apoptotic induction of cells derived from $ROCK1^{nc/nc}$ mice exhibited a lack of plasma membrane blebbing and an impairment in the proteolytic cleavage of ROCK1 (fig. S3, C and D) and a further decrease in the already low levels of thymocyte ApoBD formation (Fig. 2C and fig. S3F). Unexpectedly, the number of ApoBDs generated by $ROCK1^{wt/wt}$ and $ROCK1^{nc/nc}$ thymocytes following dex-induced apoptosis in vivo was comparable and also higher when compared to in vitro dex treatment (Fig. 2, C and D, and fig. S3G). This finding suggests that ApoBDs can be efficiently generated from apoptotic thymocytes in vivo, even in the absence of caspase-mediated activation of ROCK1.

Consistent with previous studies (*19*, *46*), inhibition of PANX1 activation during apoptosis promoted the formation of thymocyte-derived ApoBDs in vitro (Fig. 2E and fig. S3H). However, the amount of ApoBDs detected in the thymus was comparable between $PANX1^{wt/wt}$ and $PANX1^{nc/nc}$ mice when apoptosis was induced in vivo (Fig. 2F and fig. S3I). These data suggest that, although PANX1 may negatively regulate apoptotic cell disassembly in vitro, apoptotic thymocytes can efficiently disassemble into ApoBDs in vivo despite PANX1 activation. Collectively, these results indicate that in vivo apoptotic cell fragmentation is independent of the intrinsic caspase-mediated activation of ROCK1 and PANX1 in the thymic environment and suggests that there are likely additional factors present in vivo that aid cell fragmentation.

In vivo apoptotic cell fragmentation occurs in close proximity to resident phagocytes

The thymus contains multiple different cell types, including medullary and cortical epithelial cells, dendritic cells, macrophages, fibroblasts, and endothelial cells that participate in thymocyte differentiation (*48*), as well as phagocytic leukocytes that are recruited to apoptotic thymocytes to aid cell clearance (*8*, *37*, *42*, *49*). To investigate whether certain residential or recruited cell types are involved in apoptotic thymocyte fragmentation, we first monitored the immune cell infiltration into the thymus during apoptosis progression by flow cytometry. While ApoBDs begin to accumulate 4 hours post–dex treatment (Fig. 1C), it takes 9 hours for professional phagocytic immune cells, such as neutrophils, to be recruited to the thymus (Fig. 2G). Similar results were also observed when apoptosis was induced by irradiation, whereby ApoBD formation occurred before the massive infiltration of immune cells (fig. S4A). Confocal microscopy on optically cleared thymic samples demonstrated that apoptosis was primarily induced in the outer cortex of the thymus, where the main stromal populations were thymic epithelial cells (TECs), with a minor contribution of other phagocytic cells including macrophages and fibroblasts (Fig. 2H and fig. S4B). Other cell types including dendritic cells predominately localized to the medulla (Fig. 2H). A spatial analysis of the location of apoptotic particles indicated that they are not randomly distributed throughout the tissue. $CC3^+$ particles were predominantly found close to the surface of cortical TECs, macrophages, and fibroblasts, with the median shortest distance of $CC3^+$ particles to the surface of these cells being 9.41, 10.79, and 13.64 μm, respectively (Fig. 2, I and J). Dendritic cells were found further away from apoptotic fragments (29.08 μm) (Fig. 2J). Together, these results suggest that thymocyte ApoBD formation precedes the recruitment of immune cells into the thymus, and apoptotic fragments are spatially located in close proximity to residential phagocytes.

Non–cell-autonomous apoptotic cell disassembly in the zebrafish embryo

To explore the participation of resident phagocytes in the generation of ApoBDs in greater detail, we took advantage of the zebrafish embryo model that allows for in vivo imaging of cell death and clearance dynamics with unparalleled resolution. We previously showed that endogenous apoptotic cell death and phagocytic clearance play essential roles in eliminating defective cells during early zebrafish embryogenesis (*18*). This model allowed us to perform high-resolution imaging of live embryos to capture the morphodynamic features of internal pluripotent cells undergoing apoptosis in vivo, along with their mechanical interactions with surface epithelial phagocytes (Fig. 3, A and B). Both spontaneous apoptosis and apoptosis induced by Bax overexpression (Bax^+ cells) resulted in extensive fragmentation of internal cells in the in vivo environment of the live embryo (Fig. 3, C to E, and movies S1 and S2) (*18*). Quantitative analysis of apoptotic particles revealed a progressive increase in their number and a decrease in their diameter (Fig. 3, F and G),

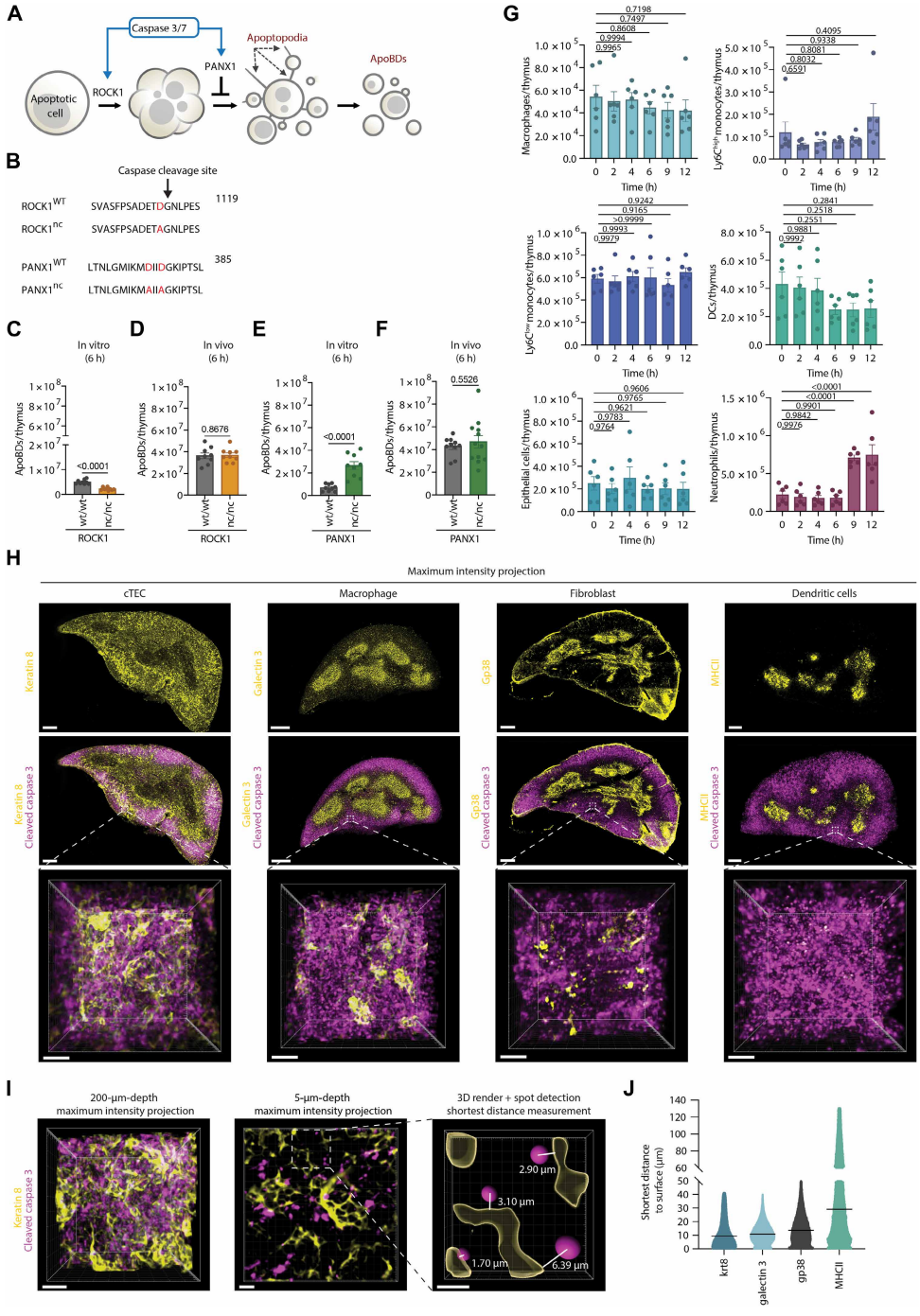

Fig. 2. Known regulators of cell-intrinsic fragmentation are not required for the formation of thymocyte-derived ApoBDs in vivo. (**A**) Schematic of the role of caspase-activated proteins in regulating ApoBD formation. (**B**) Point mutations introduced at the caspase cleavage site of ROCK1 and PANX1 proteins to prevent caspase activation. (**C** and **D**) Flow cytometry analysis of ApoBDs formed per thymus from ROCK1$^{wt/wt}$ and ROCK1$^{nc/nc}$ mice 6 hours post–dex (50 µM) treatment in vitro (C) or 6 hours post–dex (12.5 mg/kg) treatment in vivo (D) ($n = 9$). (**E** and **F**) Flow cytometry analysis of ApoBDs formed per thymus from PANX1$^{wt/wt}$ and PANX1$^{nc/nc}$ mice following 6 hours post–dex (50 µM) treatment in vitro ($n = 9$) (E) or 6 hours post–dex (12.5 mg/kg) treatment in vivo ($n = 10$ to 12) (F). (**G**) Flow cytometry analysis of total macrophages, Ly6C^{high} and Ly6C^{low} monocytes, dendritic cells, epithelial cells, and neutrophils in the thymus following 0 to 24 hours of dex (12.5 mg/kg in vivo) treatment ($n = 6$). (**H**) Representative maximum intensity projection images of cleared thymic tissue sections 6 hours post–dex (12.5 mg/kg in vivo) treatment, immunolabeled with CC3, keratin 8 [cortical epithelial cells (cTECs)], galectin 3 (macrophages), gp38 (fibroblasts), and MHCII (dendritic/antigen presenting cells). Scale bars, (whole-organ images) 300, 500, 300, and 200 µm, respectively, and (zoomed images) 20 µm. Data representative of ($n = 3$). (**I** and **J**) Analysis of the shortest distance of CC3^{+} particles from the surface of krt8^{+} ($n = 46{,}243$ particles), galectin 3^{+} ($n = 213{,}054$ particles), gp38^{+} ($n = 55{,}775$ particles), and MHCII^{+} ($n = 68{,}954$ particles) from (H). Medians are indicated (J). Scale bars, 20, 10, and 5 µm, respectively (I). All error bars represent SEM. Unpaired *t* test was performed for [(C) to (F)], and one-way ANOVA followed by Dunnett's multiple comparisons was performed for (G) to determine the indicated *P* value. h, hours.

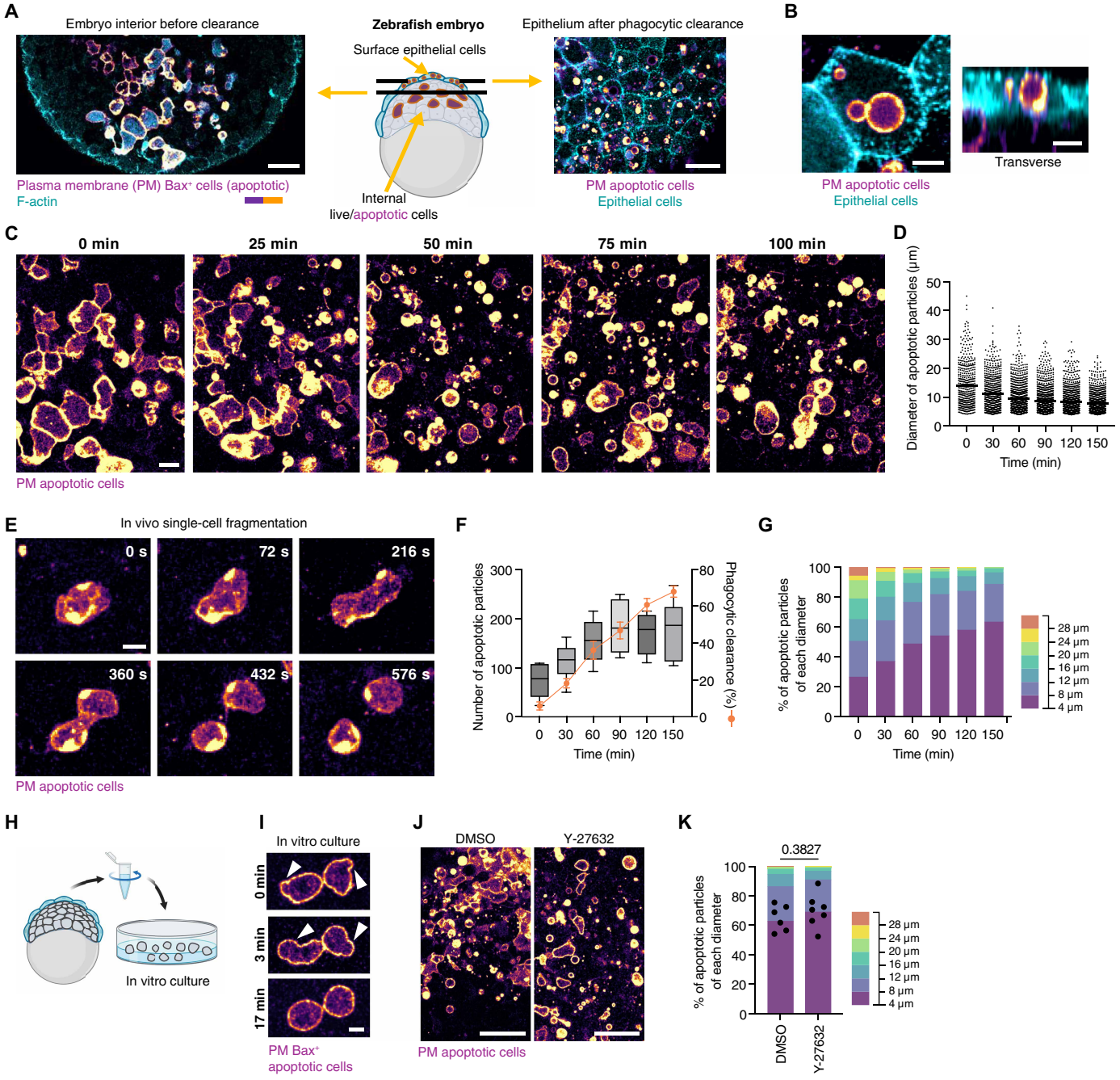

Fig. 3. In vivo fragmentation of apoptotic cells in the zebrafish embryo. (**A**) Schematics of the early zebrafish embryo during phagocytosis of apoptotic cells. Left: Embryo interior with apoptotic cells (violet-orange scale, coexpressing Bax and Lyn-TdTomato) before phagocytic clearance. Right: Superficial epithelial cells (cyan, junctions) with phagocytosed apoptotic cells. (**B**) A single epithelial cell that ingested apoptotic cells. [Created in BioRender. Hoijman, E. (2025) https://BioRender.com/7p0n15p]. (**C**) Maximum *z*-projections of two sections from a time lapse showing apoptotic cell fragmentation inside the live embryo. (**D**) Diameter of apoptotic particles over the course of fragmentation. Each dot corresponds to a single particle ($n = 6$ embryos, 443 to 1100 particles). Means are also shown. (**E**) An individual apoptotic cell fragmenting in vivo. (**F**) Number of apoptotic particles per embryo and progression of phagocytic clearance ($n = 6$ embryos). Box plot shows the maximum and minimum (whiskers), medians (lines), and 25th and 75th percentiles (boxes). For phagocytosis, means and SEM are shown. (**G**) Relative distribution of particle sizes over time ($n = 6$ embryos). (**H**) Schematics of the in vitro cultures of apoptotic embryonic cells. [Created in BioRender. Hoijman, E. (2025) https://BioRender.com/u3rncr0]. (**I**) Dynamics of Bax$^+$ apoptotic cell morphology in vitro. Arrowheads indicate blebs. Rounded cells (17 min) do not bleb anymore and do not fragment even 100 min later. (**J** and **K**) Images of cell fragmentation and distribution of particle diameters in embryos incubated with vehicle [dimethyl sulfoxide (DMSO)] or the ROCK1/2 inhibitor Y-27632 ($n = 6$ or 7 embryos, respectively). Dots correspond to the mean percentage of 4- to 8-µm particle size per embryo. Unpaired *t* test followed by Welch's correction. Embryos are Tg(*actb2:Lifeact-GFP*) in (A) to (C), Tg(*actb1:Myl12.1-eGFP*) in (J), fusion proteins expressed ubiquitously, and Tg(*Krt18:Gal4FF*) in (B), Lifeact-GFP expressed only in some epithelial cells. Scale bars, 50 mm [(A) and (J)], 10 mm [(B), (E), and (I)], and 20 mm (C).

resulting in only 2% of intact apoptotic cells (>19 um) and 71% of small fragments (<9 μm, i.e., ApoBDs) within 2.5 hours.

To evaluate the importance of the in vivo environment for apoptotic cell fragmentation, we isolated and cultured internal cells of the embryo in vitro (Fig. 3H). Similar to human pluripotent cells, these cells generate blebs even when alive both in vivo and in vitro (fig. S5A) (*50*, *51*); however, apoptosis strongly increased blebbing activity (Fig. 3I and movie S3). Time-lapse imaging of individual apoptotic cells revealed that apoptotic cells do not undergo fragmentation in vitro (zero fragmentation events in 115 apoptotic cells from three experiments) (Fig. 3I and movie S3). Comparable to the thymocyte model, targeting ROCK pharmacologically by incubating live embryos with the ROCK1/2 inhibitor Y-27632 did not interfere with the fragmentation of apoptotic cells (Fig. 3, J and K), suggesting that the intrinsic disassembly pathway is also dispensable for apoptotic cell fragmentation in the zebrafish embryo. Furthermore, overexpression specifically in apoptotic cells of dominant-negative (dn) versions of proteins that control cytoskeletal dynamics, such as Rac1, RhoA, and ROCK2 (*52*), had no effect on in vivo fragmentation (fig. S5, B and C). Together, these results indicate that apoptotic cells from zebrafish embryos rely on cell-extrinsic factors, provided in the in vivo context, for ApoBD formation, similar to what was observed with the thymocyte model.

Direct interaction between apoptotic cells and neighboring phagocytes aids cell disassembly

We next sought to identify the contributors within the in vivo embryonic environment responsible for fragmenting apoptotic cells. In vitro experiments indicated that the close proximity to neighboring apoptotic cells was not sufficient to induce their fragmentation (Fig. 3I and fig. S6A), nor was it induced by their proximity to live pluripotent cells, as evidenced by cocultures of live and apoptotic cells (zero fragmentation events in 173 apoptotic cells from four experiments) (fig. S6A). Therefore, we next examined the role of phagocytic cells in the tissue. We reported previously that surface epithelial cells exhibit extensive protrusive activity upon contact with internal apoptotic cells (fig. S6, B and C) (*18*), forming phagocytic cups for ingestion (fig. S6, D and E) and elongated epithelial arms for mechanical pushing apoptotic particles (*18*). These findings suggest the potential involvement of epithelial cells, the resident phagocytes of the early embryo, in apoptotic cell fragmentation, as hypothesized for the thymic environment.

Notably, the progressive fragmentation of apoptotic cells temporally correlated with their phagocytic uptake by epithelial cells (Fig. 3F), supporting the notion that phagocytosis and cell fragmentation are somehow linked. Analysis of the diameter of phagosomes in epithelial cells (Fig. 3B), indicative of the size of ingested apoptotic particles, predominantly yielded sizes much smaller (60% in the 4- to 8-μm range at 120 min, Fig. 3G) than those of early nonfragmented apoptotic cells (~20 μm, Fig. 3A). This led us to speculate that apoptotic cells are either (i) induced to fragment by a chemical signal from epithelial cell or (ii) mechanically fragmented during interaction with epithelial phagocytes, with either scenario followed by the phagocytosis of the fragmented target.

To explore the possibility of a mechanical interaction, we conducted four-dimensional (4D) in vivo high-resolution imaging of single-cell interactions between apoptotic cells and epithelial phagocytes. We observed that F-actin accumulates specifically in the region of the apoptotic cell where fragmentation occurs (Fig. 4A, fig. S6F, and movie S4). Even before successful fragmentation occurred, these accumulations were associated with local deformations of the apoptotic cell surface, suggesting that F-actin exerts forces driving these shape changes (movie S5). Expression of the F-actin reporter exclusively in epithelial cells indicated that these fragmentation-associated actin enrichments were not present inside the apoptotic cell but were, instead, part of protrusions from epithelial cells (fig. S6F and movie S6). High-resolution imaging allows us to visualize the dynamic 3D organization of actin filaments inside the protrusions during fragmentation in the live embryo (movie S7). These findings reveal the presence of an extrinsic compressive force applied by epithelial cells to "split" the apoptotic cell in two parts. All fragmentation events in individually tracked cells were locally enriched with F-actin (86 fragmentation events from six embryos), suggesting that fragmentation is actin dependent and primarily performed by epithelial cells.

Apoptotic cell fragmentation generated via this cell-extrinsic process was either ingested (Fig. 4A and movie S4) or not ingested (fig. S6G and movie S8) at similar frequencies (42 of 86 and 44 of 86, respectively). This demonstrates that the engagement of phagocytic protrusions with apoptotic cells can lead to apoptotic cell fragmentation, regardless of downstream phagocytic uptake events. Notably, this process occurs iteratively, leading to the generation of multiple apoptotic fragments from a single apoptotic cell (Fig. 4B and movie S9). Our quantification of single events allowed us to track the ingestion of 95 apoptotic fragments generated by 86 fragmentation events from 23 cells (at least 4.1 ± 0.3 fragments generated from 3.7 ± 0.3 fragmentation events per apoptotic cell), resulting in a mean fragmented particle diameter of 10.7 ± 0.4 μm (approximately half the size of the original apoptotic cell). These results provide a rational explanation for apoptotic cell fragmentation observed in vivo, revealing an emergent ability of epithelial cells to directly fragment apoptotic particles during and before ingestion.

To examine the mechanisms for apoptotic cell fragmentation, we injected the protein A5 inside the embryo to mask the key eat-me signal, PtdSer, on apoptotic cells as PtdSer recognition is necessary for epithelial phagocytosis (*18*). This blockade significantly reduced apoptotic cell fragmentation (Fig. 4, C and H), indicating that recognition of PtdSer on the apoptotic cell surface by epithelial protrusions is required for the fragmentation process. Similarly, modulators of phagocytosis and its associated protrusions (*18*, *53*) such as the ubiquitous expression of a dnRac1 in the embryo and the pharmacological inhibition of actin nucleation by ARP2/3 and formins with CK666 and SMIFH2 inhibitors, respectively, also inhibited apoptotic cell fragmentation (Fig. 4, D to F and H). Collectively, these results further support the key role of actin in this cell-extrinsic apoptotic cell fragmentation process. Using LY294 to inhibit PI3K, another molecule required for phagocytosis in the embryo (*18*), only mildly reduced fragmentation (Fig. 4, G and H). This is consistent with its role in the final step of uptake, the closure of the phagocytic cup, potentially allowing the maintenance of some constricting forces mediating fragmentation. Conversely, interferences that do not affect phagocytic uptake, such as the expression of dn proteins only in apoptotic cells (*18*), did not affect apoptotic cell fragmentation, as mentioned above (fig. S5, B and C).

Together, these findings demonstrate that the fragmentation of zebrafish apoptotic embryonic cells is mechanically driven by phagocytic protrusions from epithelial cells. Combined with the results obtained in the thymus, this reveals a non–cell-autonomous mechanism operating in vivo that ensures the fragmentation of apoptotic cells.

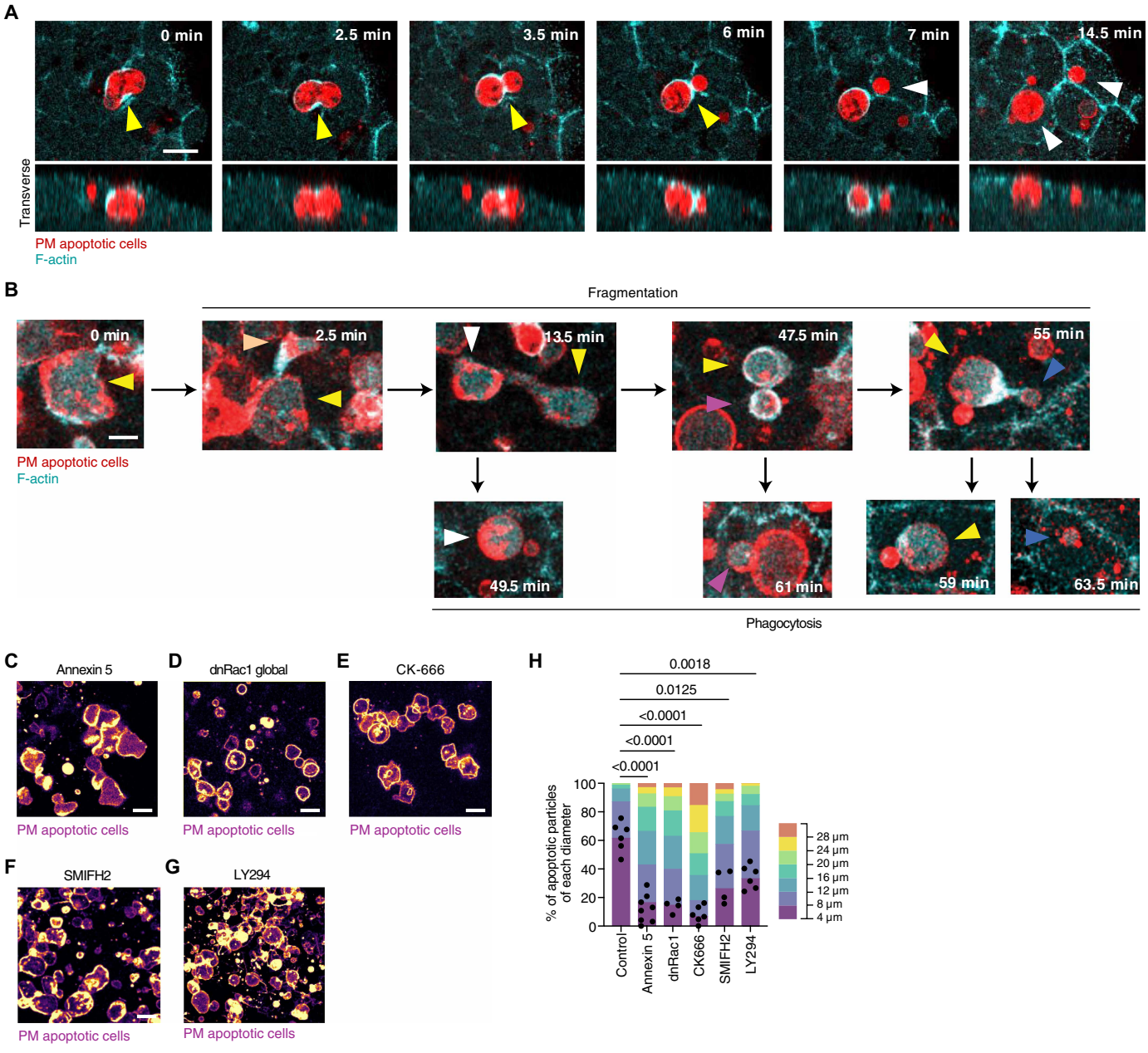

Fig. 4. Epithelial phagocytes fragment apoptotic cells. (**A**) Time-lapse microscopy showing the in vivo fragmentation of an apoptotic cell during the simultaneous phagocytic uptake by two epithelial cells. Yellow arrowheads indicate the region of F-actin accumulation. White arrowheads indicate the completion of the phagocytic event. (**B**) Single cell (yellow arrowheads) tracked over the consecutive events of apoptotic fragmentation (2.5, 13.5, 47.5, and 55 min). The top images show the first appearance of each apoptotic particle generated by a fragmentation event (orange, white, magenta, and blue arrowheads), and the bottom ones the later successful phagocytosis of those particles. The fragments are phagocytosed by multiple epithelial cells. (**C** to **H**) Maximum projection of representative images for cell fragmentation (C to **G**) and distribution of particle diameters (H) for embryos injected with A5 AF488 [(D), $n = 8$ embryos], expressing dnRac1 in all cells [(E), $n = 4$ embryos], or incubated with CK-666 [(**F**), $n = 6$ embryos], SMIFH2 [(G), $n = 4$ embryos], or LY294 [(H), $n = 6$ embryos]. In (H), dots correspond to the mean percentage of 4- to 8-µm particle size per embryo. Brown-Forsythe and Welch's ANOVA followed by Dunnett's T3 multiple comparisons test was performed to determine the indicated *P* value for the mean percentage of 4- to 8-µm particle size. Embryos shown are Tg(*actb2:Lifeact-GFP*). Scale bars, 20 µm [(A) and (C) to (G)] and 10 µm (B).

Non–cell-autonomous apoptotic cell fragmentation aids phagocytic clearance

To evaluate the functional role of the cell-extrinsic mechanism of apoptotic cell fragmentation, we focused on apoptotic particle size and performed individual and population quantifications of fragmentation and phagocytosis by the embryonic epithelium. At the tissue level, measurements of the diameter of noningested apoptotic particles during fragmentation showed a continuous decrease in their mean size over time (Fig. 5A). In contrast, ingested particles exhibited a relatively constant mean size of ~7 to 7.5 µm (Fig. 5B), with a subtle tendency to grow over time, likely reflecting the initially faster ingestion of smaller particles (fig. S7A). This value remains

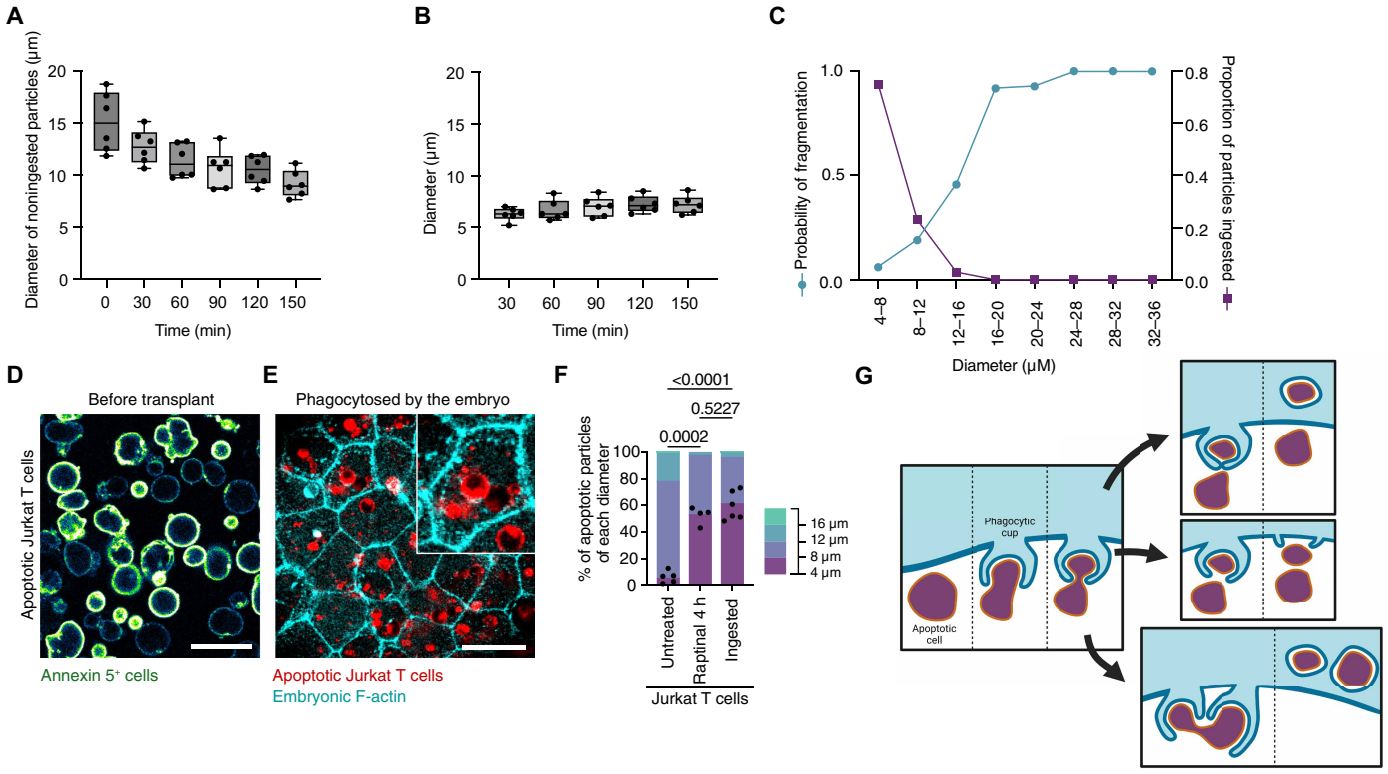

Fig. 5. In vivo apoptotic fragmentation and phagocytosis are size sensitive. (**A** and **B**) Temporal evolution of the diameter of noningested (A) and ingested (B) apoptotic particles ($n = 6$ embryos). Box plot shows the maximum and minimum (whiskers), medians (lines), and 25th and 75th percentiles (boxes), with each dot corresponding to the mean diameter per embryo. (**C**) Frequency of fragmentation or successful ingestion events of apoptotic particles of different diameters (n = fragments derived from 24 apoptotic cells from five embryos). (**D** to **F**) Ingestion of prefragmented apoptotic Jurkat T cells transplanted into Tg(*actb:Lifeact-GFP*) zebrafish embryos. (D) Fragmentation of Jurkat T cells treated with raptinal for 4 hours (4 h) before transplantation. Apoptosis was identified with A5 AF488 staining. (E) Representative images of apoptotic Jurkat T cell–derived particles ingested by the embryonic epithelium after transplantation are shown at the tissue level. A detail of a single cell that phagocytosed Jurkat T cells is also shown (inset). (F) Distribution of particle diameters from live (294 cells), apoptotic (before transplantation, 436 particles), and phagocytosed Jurkat T cells (510 particles from six transplanted embryos). Dots correspond to the mean percentage of 4- to 8-µm particle size per embryo. Brown-Forsythe and Welch's ANOVA followed by Dunnett's T3 multiple comparisons test was performed to determine the indicated P value for the mean percentage of 4- to 8-µm particle size. (**G**) Schematic diagram of epithelial protrusions fragmenting apoptotic cells. Fragmentation can result in the phagocytosis of only one (top), both (bottom), or none (middle) of the generated particles. Figure created in BioRender. Hoijman, E. (2025) https://BioRender.com/imfly5g. Scale bars, 20 µm (D) and 50 µm (E).

constant despite the initial large size of unfragmented apoptotic cells (~20 µm) and their progressive reduction in size over time (Fig. 5A). Considering the ability of the epithelium to fragment particles during ingestion, these observations suggest that the size of ingested particles is independent of the original target size and is determined by the "splitting" of apoptotic cells by epithelial cells.

To gain more insight into the coupling between apoptotic cell fragmentation and ingestion, we tracked individual apoptotic particles during this process to dynamically monitor their size changes. This quantification indicated that all apoptotic particles larger than 20 µm were fragmented, and, for those smaller than 20 µm, the probability of fragmentation decreased with the particle diameter (Fig. 5C). This analysis revealed that fragmentation is size sensitive, with larger apoptotic particles fragmenting more than smaller ones. Inversely, the probability of ingestion for each particle was higher for small particles (Fig. 5C). These results provide further evidence that the generation of small apoptotic particles is likely critical for efficient phagocytosis in vivo and is consistent with previous findings under in vitro settings (*21*). Furthermore, while the probability of fragmentation increased continuously up to 20 µm, ingestion becomes limited for particles larger than 12 µm (Fig. 5C). This suggests a threshold for ingestion and thus an optimal size of apoptotic fragments (<8 µm, about 2.5 times smaller than the size of a nonfragmented apoptotic cell) for efficient phagocytosis.

To test this hypothesis experimentally, we injected prefragmented apoptotic particles into the zebrafish embryo to determine whether they are further fragmented or directly ingested by epithelial cells. Given that zebrafish cells do not fragment autonomously, we used apoptotic human Jurkat T cells, previously shown to be efficiently phagocytosed by the embryonic epithelium (*18*). We promoted intrinsic fragmentation by treating these cells with the apoptosis inducer and PANX1 inhibitor raptinal (*46*, *54*, *55*) (Fig. 5D). This generated apoptotic particles with a mean diameter of 7.9 ± 0.1 µm (n = 436 fragments from four experiments) (Fig. 5F). After transplantation into the embryo, apoptotic Jurkat cell fragments were phagocytosed without additional fragmentation (Fig. 5E), supporting that, once fragments reach sizes appropriate for ingestion, further fragmentation does not occur. The efficient clearance observed

for the intrinsically fragmented Jurkat T cells would be thus generated by the combination of a low fragmentation probability for particles of these sizes and a high ingestion probability.

Last, we investigated the fate of apoptotic cells when their interactions with epithelial phagocyte protrusions were disrupted. A time-course analysis of apoptotic cells isolated from the embryo interior before phagocytosis begins and maintained in culture revealed a progressive increase in secondary necrosis (fig. S7B and movie S10). Likewise, in vivo blockade of epithelial-apoptotic cell interactions by injecting A5 into the embryo led to an increased number of secondary necrotic cells (fig. S7C). These findings underscore the critical role of efficient apoptotic cell clearance in preventing the accumulation of necrotic cells within the embryo, which could pose a risk to normal development.

Together, these results support the concept that cell-extrinsic fragmentation ensures that apoptotic particles are remodeled to sizes small enough to be efficiently removed by the phagocytic epithelium, which has an intrinsic limit size for proficient ingestion.

DISCUSSION

In this study, we reveal an in vivo cell-extrinsic process of fragmentation acting on apoptotic cells that do not exhibit clear cell-intrinsic fragmentation (Fig. 5G). Given the high clearance efficiency observed in the tissues studied, this cell-extrinsic fragmentation process appears sufficient to address the challenge of ingesting large apoptotic cells and optimizing clearance tasks. This cell-extrinsic mechanism offers the advantage of fragmenting apoptotic cells in close proximity to phagocytes and at the time that they are ready for clearance. Thus, it might prevent the formation of small fragments in inappropriate locations or times, which could delay clearance, potentially allowing these fragments to transition into necrotic particles and trigger inflammatory responses.

Although cell-intrinsic fragmentation is widely accepted as a core mechanism of the apoptotic program, our results suggest that its relevance in physiological settings requires further exploration. It is possible that different apoptotic subprograms exist, with some involving cell-intrinsic fragmentation and others not, depending on the specific biological setting in which these cells are cleared. Alternatively, the cell-intrinsic fragmentation observed in some cultured cells as shown here with the PANX1$^{nc/nc}$ mice could be a backup response activated when phagocytes are unable to perform cell-extrinsic fragmentation. However, while we observed the cell-extrinsic mechanism operating in two different biological contexts, it remains to be determined whether this mechanism is ubiquitous or specific to certain tissue contexts. Our observation that zebrafish cells undergo blebbing but not cell-intrinsic fragmentation challenges the general association between these two processes (*24*), suggesting that cell-intrinsic fragmentation may not be an inevitable consequence of blebbing. Instead, blebbing may play other roles in apoptotic cells, such as the recent claim that blebs present surface molecular features serving as platforms for initiating phagocytosis (*56*) or providing local mechanical features to aid cell-extrinsic fragmentation.

The dual mechanism of fragmentation and phagocytosis performed simultaneously by phagocytes would create a synergy that accelerates clearance. These phagocytic cells generate their own small fragments to produce particle sizes that can be more effectively managed during clearance. This process does not just apply to individual cells; noningested fragments generated by one phagocyte can be phagocytosed by neighboring cells, highlighting the cooperative nature of tissue clearance (*18*). The advantage of phagocytosing smaller objects may be related to the mechanics of the process (*15*). For instance, the curvature of the plasma membrane protruding to form a large phagocytic cup could be a limiting factor (*57*–*59*). Additionally, the extent to which the phagocytic cell must deform to accommodate large apoptotic particles could be more challenging for epithelial cells than for professional phagocytes, given their stable insertion inside a tissue layer of defined geometry (*60*). These mechanical constraints might explain the size reduction we observed, with most ApoBDs reaching ~2.5 times smaller than the size of the intact apoptotic cell before phagocytosis. Additionally, the availability of specific molecules recruited to large protrusions or vesicles after ingestion could also influence the size of the ingested objects, either because there is a limited amount of these molecules available per cell or because they are redistributed from other locations, such as actin from epithelial cell junctions (*18*).

Our results unmask a mechanism in which one cell breaks another into multiple equal parts, remodeling it to achieve smaller sized particles (Fig. 5G). While other immune cells can ingest fragments of large cells through trogocytosis, this process was primarily associated with intercellular communication (*61*, *62*). The fact that cell-extrinsic fragmentation occurs extensively in certain tissues and facilitates cell clearance provides a distinct viewpoint to the operation of phagocytes. The actin enrichments involved in cell-extrinsic fragmentation parallel the compressing rings observed in phagocytic cups, which propel apoptotic particles into the cell interior (*18*, *63*). Accordingly, it has been proposed that these localized forces may be sufficient to split a cell into two parts (*53*). The constricting structures observed during fragmentation might also be related to cytokinetic rings, which divide one cell into two during cell division, although these rings rely on myosin II–generated forces (*64*) and are precisely localized to ensure the proper inheritance of cellular components between the two daughter cells (*65*). According to our time-lapse analysis, the exact site of cell-extrinsic fragmentation of apoptotic cells does not appear to be fixed, although we cannot rule out the presence of unknown factors that determine the localization of cell fragmentation machineries.

Our study captured previously unrecognized subcellular dynamics during tissue clearance in vivo, revealing that phagocytes in the local microenvironment fragment apoptotic cells into ApoBDs to facilitate their removal. This adds a different perspective to the classical view of a fundamental step in the apoptotic program and may guide the development of therapies to control apoptotic cell clearance in phagocytosis-associated diseases (*66*).

MATERIALS AND METHODS

Reagents

Dexamethasone (D4902) and Hoechst 33342 were purchased from Sigma-Aldrich. TO-PRO-3 (T3605), collagenase type 1 (17100017), and Vybrant FLICA Caspase Apoptosis Assay Kits for flow cytometry (V35118) were purchased from Thermo Fisher Scientific. Anti-mouse Ly6C BV421 (clone AL-21; 562727), anti-mouse CD4 BV510 (clone RM4-5; 563106), anti-mouse CD8a BV510 (clone 53-6.7; 563068), anti-mouse I-A/I-E BV650 (clone 2G9; 743873), anti-mouse CD11c phycoerythrin (clone HL3; 557401), anti-mouse Ly6G allophycocyanin (clone 1A8; 560599), anti-mouse CD45.2 AF700 (clone 104; 560693), purified rat anti-mouse CD16/CD32 (mouse BD Fc Block) (clone

2.4G2; 553142), A5 fluorescein isothiocyanate (FITC; 556419), A5 BV605 (563974), and 10× A5 binding buffer (556454) were purchased from BD Biosciences. Anti-mouse F4/80 PE/Cyanine5 (clone BM8; 123112) and anti-mouse CD326 (Ep-CAM) APC/Cyanine7 (clone G8.8; 118218) were purchased from Australian Biosearch. Anti-mouse CD11b PE-Cyanine7 (clone M1/70; 25-0112-82), anti-mouse CD8a PE (clone 53-6.7; 12-0081-82), and anti-mouse CD4 PE-Cyanine7 (clone RM4-5; 25-0042-82) were purchased from eBioscience. SPHERO AccuCount blank particles of 5.0 to 5.9 μm (ACBP-50-10) were purchased from Spherotech.

Cell culture

Mouse embryonic fibroblasts (MEFs) derived from E14.5 wild-type and ROCK1^{nc} embryos were immortalized with SV40 large T antigen (a gift from Puthalakath laboratory, La Trobe University) and maintained in high-glucose Dulbecco's modified Eagle's medium (DMEM) containing 10% (v/v) fetal bovine serum (FBS; Scientifix), penicillin (50 U/ml), and streptomycin (50 μg/ml), at 37°C in 5% CO_2. Murine thymocyte suspensions were maintained in RPMI medium containing 10% (v/v) FBS (Scientifix), penicillin (50 U/ml), and streptomycin (50 μg/ml), at 37°C in 5% CO_2. For zebrafish transplantation experiments, human acute leukemic Jurkat T cells (clone E6-1, American Type Culture Collection, Bethesda, MD, USA) obtained from A. Jordan (Institute of Molecular Biology of Barcelona) were maintained in RPMI 1640 medium supplemented with 10% (v/v) fetal calf serum, penicillin (100 U/ml) and streptomycin (100 mg/ml), sodium pyruvate (110 mg/liter), and 2 mM L-glutamine, at 37°C in 5% CO_2. Cells were treated with 10 μM Raptinal for 4 hours, washed in DMEM (DMEM/F-12 with L-glutamine and Hepes, Sigma-Aldrich), and stained with FM 4-64FX (5 μg/ml; Thermo Fisher Scientific) for 5 min. Cells were then transplanted into 4-hour-postfertilization Tg(actb1:Lifeact-GFP) embryos with a CellTram Vario (Eppendorf) and live imaged after 3 hours. An aliquot of cells was stained with A5 AF488 before transplantation and imaged to confirm apoptosis and analyze fragmentation. The cells were tested negative for mycoplasma contamination and authenticated morphologically.

Generation of PANX1 caspase noncleavable mice

Generation of ROCK1 caspase noncleavable mice was described in (*44*) and backcrossed nine times. PANX1 caspase noncleavable mice were generated by CRISPR-Cas9 as previously described (*67*). Briefly, one single guide RNA with the sequence of ATTAAGATGGACATCATTGA, an oligo donor with the sequence AGCAATGGGCAGGGCATTGA-CCCCATGCTACTCCTGACAAACCTGGGCATGATTAAGATG-gccATCATTgccGGAAATTCCCACGTCCCTACAGACCAAG-GGAGAGGACCAGGGCAGCCAGAGAGTGAGTT, and Cas9 mRNA were injected into the cytosol of C57bl/6J zygotes. Mice were backcrossed three times to minimize off-target mutations, and mutations were confirmed by Sanger sequencing. Due to PANX1 having multiple caspase cleavage sites, PANX1 channel activity during apoptosis was determined using a functional assay, whereby apoptotic thymocytes were stained with TO-PRO-3 and analyzed by flow cytometry as described below. Lack of TO-PRO-3 uptake is indicative of inactive PANX1 channels. Littermate controls were used for experiments using ROCK1^{nc} and PANX1^{nc} mice.

In vivo model of thymocyte apoptosis

Five- to 7-week-old C57Bl/6 mice (male and female) were maintained and used under approval of AEC21034, La Trobe University. All methods and experiments were approved by the La Trobe University Animal Ethics Committee in accordance with the National Health and Medical Research Council Australia code of practice for the care and use of animals for scientific purposes. To induce apoptosis in vivo, mice were intraperitoneally injected with dex (12.5 mg/kg) as previously described (*19*). Whole-body x-ray irradiation was performed using the Rad Source RS-2000 X-Ray Irradiator (Rad Source Technologies Inc.). Mice were housed in an Allentown cage and exposed to 6.8 gray (Gy). Following irradiation, mice were euthanized by CO_2 and thymi were harvested and processed for flow cytometry or tissue clearing as described below.

In vitro model of MEFs and thymocyte apoptosis

MEFs were treated with 5 μM ABT737/10 μM S63845 and incubated at 37°C for 4 hours. Primary thymocytes derived from wild-type, ROCK1^{nc}, and PANX1^{nc} mice were treated with 50 μM dex and incubated at 37°C for 6 hours.

Flow cytometry

Single-cell thymocyte suspensions were generated by resuspending the thymus in collagenase type I (1 mg/ml) for 20 min at room temperature (RT). EDTA was added for a final concentration of 12 mM and resuspended for a further 5 min on ice. Cell suspensions were pelleted at 3000*g* for 5 min, then resuspended in RPMI medium containing 10% (v/v) FBS, and strained through 70-μm cell strainer. For cell viability analysis, thymocyte suspensions were stained with anti-mouse CD4 PE-Cy7 (1:300), anti-mouse CD8α PE (1:300), A5 FITC (1:100), TO-PRO-3 (1:2000), and Hoechst 33342 (1:2000) diluted in 1× A5 binding buffer at RT for 10 min. For analysis of active caspase 3/7, samples were stained with Vybrant FAM (FLICA) as per the manufacturer's instructions, followed by anti-mouse CD4 PE-Cy7 (1:300), anti-mouse CD8α PE (1:300), A5 BV605 (1:100), TO-PRO-3 (1:2000), and Hoechst 33342 (1:2000) diluted in 1× A5 binding buffer at RT for 10 min. For quantification of immune cell populations, thymocyte suspensions were stained with purified rat anti-mouse CD16/CD32 (mouse BD Fc Block; 1:300), anti-mouse Ly6C BV421 (1:300), anti-mouse CD4 BV510 (1:300), anti-mouse CD8a BV510 (1:300), anti-mouse I-A/I-E BV650 (1:300), anti-mouse CD11c PE (1:300), anti-mouse Ly6G APC (1:300), anti-mouse CD45.2 AF700 (1:300), A5 BV605 (1:100), anti-mouse F4/80 PE/Cyanine5 (1:150), anti-mouse CD326 (Ep-CAM) APC/Cyanine7 (1:300), and anti-mouse CD11b PE-Cyanine7 (1:300) diluted in FACS buffer [10% (v/v) FBS, 2 mM EDTA, phosphate-buffered saline (PBS), 1× A5 binding buffer] at 4°C for 20 min. Flow cytometry analysis was performed using BC CytoFLEX S (Beckman Coulter) or BD FACS Canto II (BD Biosciences), and data were analyzed by FlowJo software version 10.8.2.

Immune cell populations were defined by flow cytometry as follows: macrophages, CD45.2$^+$/CD11b$^+$/Ly6G$^-$/F480$^+$; Ly6C^{high} monocytes, CD45.2$^+$/CD11b$^+$/Ly6G$^-$/F480$^-$/Ly6C^{high}; Ly6C^{low} monocytes, CD45.2$^+$/CD11b$^+$/Ly6G$^-$/F480$^-$/Ly6C^{low}; dendritic cells, CD45.2$^+$/CD11b$^+$/CD11c$^+$/MHCII$^+$; epithelial cells, CD45.2$^-$/EpCAM$^+$; and neutrophils, CD45.2$^+$/CD11b$^+$/Ly6G$^+$.

Immunoblotting

Thymocytes were lysed in lysis buffer [1% IGEPAL CA-630, 10% glycerol, 1% Triton X-100, 150 mM NaCl, 20 mM Hepes (pH 7.4), and protease inhibitor cocktail tablet (Roche)] and analyzed by SDS-PAGE. Immunoblotting was performed using the following

antibodies: rabbit anti-ROCK1 (1:100; Santa Cruz), mouse anti-β-actin (1:4000; Sigma-Aldrich), HRP-conjugated sheep anti-mouse IgG (1:5000; GE Healthcare), and HRP-conjugated goat anti-rabbit IgG (1:5000; Invitrogen).

Transmission electron microscopy

Thymi were harvested and placed directly into 4% paraformaldehyde (PFA) to initiate sample fixation. Lobes were dissected into smaller sections using a scalpel blade and transferred into Karnovsky's fixative [2.0% (v/v) PFA/2.5% (v/v) glutaraldehyde in phosphate buffer] and incubated overnight at 4°C. Samples were washed with 1 M sodium cacodylate buffer (pH 7.4) for 5 min before postfixing with 2% (w/v) osmium tetraoxide and 1.5% (w/v) potassium ferricyanide solution in 0.1 M sodium cacodylate (pH 7.4), for 1 hour at 4°C. Fixation, cross-linking, and staining processes were accelerated by using the PELCO BioWave microwave system under 100 W and vacuum settings as follows: three times for 2 min ON/OFF with osmium/potassium ferricyanide solution, three times for 2 min ON/OFF with 1% (w/v) thiocarbohydrazide and Milli-Q solution, three times for 2 min ON/OFF with 2% (w/v) osmium tetraoxide in Milli-Q, three times for 2 min ON/OFF with 2% (w/v) uranyl acetate in Milli-Q, and three times for 2 min ON/OFF with lead aspartate, with 5-min washing three times with Milli-Q between each step. Next, serial dehydration of tissue was continued at 150 W without vacuum using the following sequential steps: 40 s with 50% (v/v) ethanol, 40 s with 70% ethanol, 40 s with 90% ethanol, two times for 40 s with 100% ethanol, and lastly two times for 40 s with 100% propylene oxide. Infiltration of Araldite 502/Embed 812 resin was conducted at 250 W with vacuum, first with 25% and then with 50% propylene oxide/resin solution and lastly with 100% resin solution. Samples were replaced with fresh resin before embedding and polymerizing at 60°C for 72 hours. Serial sections (100 nm) were cut using the Leica EM UC Ultramicrotome. Samples were imaged using the Hitachi SU7000 field-emission scanning electron microscope at 2 kV and 20-nm pixel size.

Particle analysis of TEM images

Images were filtered with Gaussian blur before conducting analysis. Thymocytes and apoptotic particles (inside and outside) were manually segmented using the MultiROI tool in Dragonfly version 2022.2 Build 1409. Apoptotic particles were determined on the basis of the following parameters: small size, condensed, disrupted or ruffled nucleus, swelled mitochondria, and density. Regions of interest (ROIs) were exported as binary images, and Feret diameter was calculated using the analyzed particles feature on ImageJ (version 2.14.0).

Immunohistochemistry

Whole thymic tissue was fixed with 4% (w/v) PFA at 4°C overnight. Tissue was processed using the Tissue-Tek VIP 6 AI Tissue Processor (Sakura Finetek), and antigen retrieval was performed using the EnVision FLEX TRS, low pH (Dako) at 97°C for 30 min. Paraffin-embedded sections were immunohistochemically stained with anti–cleaved caspase 3 (clone Asp175, 1:300, Cell Signaling Technology) and counterstained with Mayer hematoxylin using the automated Omnis EnVision G2 template (Dako, Glostrup).

PACT tissue clearing

Whole thymic tissue was fixed with 4% (w/v) PFA at 4°C for 4 hours. Tissue was embedded in 3% low melting point agarose then sectioned using the Leica VT1200 vibratome. 200 μm sections were transferred to passive clarity technology (PACT) monomer solution (40% w/v acrylamide, 0.25% w/v azo-initiator, 1× PBS) and incubated at 4°C for 24 hours. Samples were processed as previously described (*68*) and then stained with the following primary antibodies for 24 hours at RT: anti–keratin 8 monoclonal antibody [clone TROMA-I; 1:300; deposited to the Developmental Studies Hybridoma Bank (DSHB) by P. Brulet/R. Kemler], anti-CD8α monoclonal antibody (1:100; clone 53-6.7; eBioscience, 14-0081-82), anti–major histocompatibility complex class II (MHCII; I-A/I-E) monoclonal antibody (1:100; clone M5/114.15.2; eBioscience, 14-5321-82), anti–galectin 3 monoclonal antibody (1:100; clone M3/38; eBioscience, 14-5301-82), and anti-podoplanin monoclonal antibody (1:200; clone 8.1.1; eBioscience, 14-5381-82). Samples were then stained with the following secondary antibodies diluted in staining buffer for 24 hours at RT: goat anti-rat immunoglobulin G (IgG; H+L) cross-adsorbed secondary antibody, Alexa Fluor 555 (AF555; 1:200; eBioscience, A-21434); goat anti-rabbit IgG (H+L) cross-adsorbed secondary antibody, AF647 (1:200; eBioscience, A-21244); and goat anti-Syrian hamster IgG (H+L) cross-adsorbed secondary antibody, AF488 (1:200; eBioscience, A-21110). Samples were washed with 0.1% (v/v) Triton X-100 in PBS for 24 hours, then stained 4′,6-diamidino-2-phenylindole (1.25 μg/ml) for 6 hours, and then subsequently washed with 0.1% (v/v) Triton X-100 in PBS for 9 hours. Cleared tissue was then incubated in EasyIndex (refractive index, 1.52; LifeCanvas technologies) until translucent.

Confocal microscopy

Cleared thymic sections were mounted in EasyIndex and imaged using the Andor Dragonfly 202 Spinning Disk Confocal with 20× objective. Image processing was performed by Fusion, and data were analyzed using Imaris v9.0. For disassembly analysis of mouse thymocytes and MEFs, cells were seeded in eight-well Nunc Lab-Tek II chamber slides (Nunc, Denmark) before apoptosis induction. Image processing and data analysis were performed using Zen software (Zeiss) and Imaris Software (Bitplane AG, Switzerland) v9.5.1.

Thymic section confocal image analysis

CD4 and cleaved caspase 3 cells were segmented using the spot detection tool in Imaris to determine the overall particle count and particle diameter. Thresholds were chosen in a semiautomatic manner on the basis of green fluorescent protein (GFP; green) and Cy5 (magenta) channels for CD4 and cleaved caspase 3, respectively. Cleared tissue images were processed using Imaris, and ROIs in tissue sections are presented as maximum intensity projections of full *z*-projections.

Immune cells were segmented using surface rendering tool in Imaris. Thresholds were chosen in a semiautomatic manner on the basis of red fluorescent protein (yellow) channel. To determine the shortest distance of cleaved caspase 3 particles to the nearest neighboring immune cells, cleaved caspase 3 spots were filtered to exclude particles that are touching or inside immune cells. Cleared tissue images were processed using Imaris, and ROIs in tissue sections are presented as maximum intensity projections of 30 μm *z*-projections.

Zebrafish lines and maintenance

AB wild-type zebrafish and the following transgenic lines were used: Tg(*actb1:Lifeact-GFP*) (*69*), Tg(*actb1:Myl12.1-eGFP*) (*70*), Tg(*krt18:Gal4FF*) (*71*), and Tg(*Krt18:Gal4FF/UAS:Lifeact-GFP*) (*18*).

Fish were maintained and bred according to the standard procedures at the aquatic facility of the Parc de Bellvitge Biomedical Research Institute (IDIBELL). Embryos were kept in E3 medium at 25° to 31°C before experiments and staged on the basis of morphological criteria (*72*) and hours postfertilization. All protocols used have been approved by the Ethic Committee of Animal Experimentation (IDIBELL-CEEA), procedure AR18010, and were implemented according to national and European regulations. Females were crossed with males (between 5 and 12 months of age) to obtain eggs.

Subcellular staining of zebrafish embryos

The following mRNAs encoding fusion proteins were synthetized from pCS2$^+$ plasmids using the SP6 mMessenger mMachine kit (Ambion) and injected at different stages: H2A-mCherry (100 pg, nuclear staining) and Lyn-tdTomato and Lyn-GFP (50 pg, plasma membrane staining). To perform a mosaic expression of Lifeact-GFP specifically in epithelial cells, the Tg(*krt18:Gal4FF*) line was injected with 25 pg of plasmid DNA of pT2AUAS:Lifeact-GFP8, together with 25 pg of tol2 transposase mRNA at one-cell stage.

Zebrafish apoptotic induction and apoptotic cell staining

To induce apoptosis in zebrafish embryos, 2 pg of zbax mRNA9 (Bax$^+$ cells) was injected (together with lyn-tdTomato) at the 16- to 32-cell stage to generate mosaic embryos bearing apoptotic cells from 4 hours postfertilization when embryos were mounted for live imaging for 2 to 3 hours. To detect apoptotic cells, cells were stained with A5 AF488 (Invitrogen) in vitro. To interfere with phagocytosis or fragmentation, 10 nl of recombinant A5 was injected into the blastula cap at 4 hours postfertilization.

Expression of dn proteins in zebrafish embryos

Expression of dn proteins was performed by injection of 20 pg of dnRac1N1714 and 40 pg of dnRhoAN1914 or dnRock2a mRNA either at one-cell stage (to obtain global expression) or at 16- to 32-cell stage (to generate mosaic embryos). In some experiments, 100 pg of h2A-mCherry mRNA was coinjected to identify cells expressing dn proteins.

Pharmacological treatment of zebrafish embryos

Dechorionated embryos were incubated with 50 μM Y-27632, 50 μM LY294 (Sigma-Aldrich), 50 μM SMIFH2 (Sigma-Aldrich), 100 μM CK-666 (Tocris Bioscience), or dimethyl sulfoxide (control) in Danieu's solution for 1 to 3 hours and mounted in the presence of the corresponding drugs for in vivo imaging to analyze fragmentation and phagocytic uptake.

In vitro heterotypic culture

Cultures of zebrafish progenitor cells in vitro were prepared at 4 hours postfertilization by vortexing manually dechorionated embryos and centrifugation, and the pellet was collected in DMEM (DMEM/F-12 with L-glutamine and Hepes, Sigma-Aldrich). Cells were plated in a glass bottom dish (MatTek) for live imaging. Cells obtained from Tg(*actb1:Lifeact-GFP*) embryos injected with 5 pg of bax and 50 pg of lyn-tdTomato mRNA, and uninjected control cells were mixed in a proportion of 1:2 to prepare the cell suspension.

Detection of necrotic cells

To monitor the dynamics of secondary necrosis, one cell of the four-cell stage embryos was injected with bax and h2b-gfp mRNAs (the latter providing nuclear staining to visualize nuclear fragmentation in apoptotic cells), with the aim of generating a large number of apoptotic cells before the onset of phagocytosis. At the sphere stage, cells were isolated from embryos as described above for the in vitro cultures. The isolated cells were incubated for varying periods, stained with propidium iodide for 15 min, and imaged by confocal microscopy. In a separate set of experiments, embryos were injected at the 32-cell stage, as described above, to allow the phagocytic process to proceed under normal conditions. At the sphere stage, these embryos were injected with A5-AF488 or PBS, and phagocytosis was allowed to occur. At 7 hpf, cell suspensions were prepared and cultured for 18 hours, after which propidium iodide staining and confocal imaging were performed. The fold change A5/PBS was used to evaluate the statistical significance.

Live imaging of zebrafish embryos

Embryos were maintained in E3 medium (5 mM NaCl, 0.17 mM KCl, 0.33 mM $CaCl_2$, and 0.33 mM $MgSO_4$) until they were dechorionated and mounted in 1% low-melting point agarose in Danieau's solution [58 mM NaCl, 0.7 mM KCl, 0.4 mM $MgSO_4$, 0.6 mM $Ca(NO_3)_2$, and 5 mM Hepes] over 35-mm glass bottom dish (MatTek) and imaged with a 20× (0.8 numerical aperture) glycerol-immersion objective at 28°C on Leica TCS SP5 and Zeiss 980 confocal microscopes. Laser excitation of 488 nm and 543/561 nm and HyD detectors were used. *Z*-stacks of 0.5- to 2-μm spacing between *z*-slices were acquired with a temporal resolution of 1 s to 20 min depending on the experiment. Software used were LAS X (v3.5.5.19976) and LAS AF (v2.7.3.9723). Embryos or cultured cells were imaged at different time points during phagocytosis and fragmentation, either with individual snapshots or time lapses of images acquired every 0.5 to 20 min, depending on the process analyzed.

Image analysis of zebrafish embryos

Raw data were analyzed and quantified using Fiji software (ImageJ 1.52p). Images were processed for figure preparation by applying Gaussian blur filter. In some cases, *z*-projections were shown as indicated. For pictures illustrating global fragmentation states, maximum *z*-projections of two sections equivalent to the ones shown in Fig. 3A were used. In Fig. 4B, fig. S6 (D to F), and movies S6 and S8, regions of the images were cropped to improve visualization of a given structure. Quantification of phagocytic activity was performed using the point tool and ROI manager from *z*-stacks. Ingested apoptotic particles inside phagosomes were identified by the red signal originating from the Lyn-tdTomato marker expressed in apoptotic cells. To count phagosomes, particles smaller than 3 μm were discarded from the analysis. Apoptotic fragments not ingested by the EVL cells were identified by their red signal, an increased Lifeact-GFP signal, and their characteristic random morphology. The diameter of each phagosome was measured with the line tool, in the *z* plane corresponding to the larger area captured for that specific particle. For noningested apoptotic particles with very asymmetrical shapes, the length measured corresponded to an intermediate distance between the longer and shorter axes. The classification of apoptotic fragments as ingested or noningested was performed on the basis of 3D visualization of the localization of the fragment and, considering the spherical shape of ingested cells, different from the asymmetric morphologies of noningested ones. Necrotic cells were identified as PI$^+$, having nuclear fragmentation (analyzed by H2B-GFP expression) and varying morphological changes (swelling

and abnormal shapes). Necrotic particles larger than 12 μm were quantified to focus on the fate of apoptotic cells.

Image analysis for tracking single-cell fragmentation and ingestion in 4D

To follow the behavior of individual apoptotic cells inside the live embryo, nonfragmented apoptotic cells and all their derived fragments were tracked in 4D for 3 hours, registering the lineage of each original cell and their derived fragments. Nonfragmented apoptotic cells (diameter > 20 μm, lyn-tomato$^+$, and irregular morphology) at the beginning of the time lapse were selected if they (or they derived fragments) remain in the 3D field of view during throughout the experiment. The diameter was continuously monitored for initial nonfragmented particles and all derived fragments. Identification of successful phagocytic events was performed as described previously (*18*). Briefly, a phagocytic event involves a particle previously moving within the embryo, often changing shape, which is then enveloped by actin and drawn into the 3D space of an epithelial cell (for examples, see movie S8), which remains until its destruction (*18*). Once inside the epithelial cell, the apoptotic particle adopts the spherical or disk shape characteristic of phagosomes (see movie S8). In contrast, a fragmentation event occurs when a single particle is separated into two or more parts, each of which can be identified as an independent object (see Fig. 3E and movie S2). All individual fragmentation and phagocytic events were registered and assigned to be derived from an originally nonfragmented apoptotic particle. Therefore, the whole lineage of each initial apoptotic cell and their derived fragments, including all the fragmentation and ingestion events, were obtained. In some cases, a reduced number of apoptotic cells were transplanted from one sphere-stage embryo to another of the same genotype to enhance visualization.

Statistics and reproducibility

Raw data were visualized and processed using Microsoft Excel for Microsoft 365 v2411 and GraphPad Prism v10.0.0 (GraphPad Software Inc.). Data are presented as the means ± SEM unless otherwise stated. Statistical significance was determined using Microsoft Excel and GraphPad Prism v9.0.0 as stated in the figure legend. For all data presented, independent experiments were repeated at least three times with similar results. Sample sizes were chosen empirically with the aim to optimize the maximum number of samples per each independent experiment while also considering the 3Rs (reduction/refinement/replacement) for animal research and the experimental limitations such as the number of embryos possible to image simultaneously during in vivo acquisitions. Statistical tests were applied to evaluate the significance of the analyzed effects for the given sample sizes. Blinding was not required during data collection as standardized experimental procedures and imaging protocols were applied for different groups. Blinding during data analysis was applied when possible, involving multiple investigators with blinded datasets. Randomization was performed by using multiple parental couples for mating in each independent experiment and randomly distributing embryos into different groups.

Supplementary Materials

The PDF file includes:
Figs. S1 to S7
Legends for movies S1 to S10

Other Supplementary Material for this manuscript includes the following:
Movies S1 to S10

REFERENCES

1. S. Elmore, Apoptosis: A review of programmed cell death. *Toxicol. Pathol.* **35**, 495–516 (2007).
2. P. M. Henson, D. A. Hume, Apoptotic cell removal in development and tissue homeostasis. *Trends Immunol.* **27**, 244–250 (2006).
3. A. Hochreiter-Hufford, K. S. Ravichandran, Clearing the dead: Apoptotic cell sensing, recognition, engulfment, and digestion. *Cold Spring Harb. Perspect. Biol.* **5**, a008748 (2013).
4. S. Nagata, Apoptosis and clearance of apoptotic cells. *Annu. Rev. Immunol.* **36**, 489–517 (2018).
5. I. Vitale, F. Pietrocola, E. Guilbaud, S. A. Aaronson, J. M. Abrams, D. Adam, M. Agostini, P. Agostinis, E. S. Alnemri, L. Altucci, I. Amelio, D. W. Andrews, R. I. Aqeilan, E. Arama, E. H. Baehrecke, S. Balachandran, D. Bano, N. A. Barlev, J. Bartek, N. G. Bazan, C. Becker, F. Bernassola, M. J. M. Bertrand, M. E. Bianchi, M. V. Blagosklonny, J. M. Blander, G. Blandino, K. Blomgren, C. Borner, C. D. Bortner, P. Bove, P. Boya, C. Brenner, P. Broz, T. Brunner, R. B. Damgaard, G. A. Calin, M. Campanella, E. Candi, M. Carbone, D. Carmona-Gutierrez, F. Cecconi, F. K.-M. Chan, G.-Q. Chen, Q. Chen, Y. H. Chen, E. H. Cheng, J. E. Chipuk, J. A. Cidlowski, A. Ciechanover, G. Ciliberto, M. Conrad, J. R. Cubillos-Ruiz, P. E. Czabotar, V. D'Angiolella, M. Daugaard, T. M. Dawson, V. L. Dawson, R. De Maria, B. De Strooper, K.-M. Debatin, R. J. Deberardinis, A. Degterev, G. Del Sal, M. Deshmukh, F. Di Virgilio, M. Diederich, S. J. Dixon, B. D. Dynlacht, W. S. El-Deiry, J. W. Elrod, K. Engeland, G. M. Fimia, C. Galassi, C. Ganini, A. J. Garcia-Saez, A. D. Garg, C. Garrido, E. Gavathiotis, M. Gerlic, S. Ghosh, D. R. Green, L. A. Greene, H. Gronemeyer, G. Häcker, G. Hajnóczky, J. M. Hardwick, Y. Haupt, S. He, D. M. Heery, M. O. Hengartner, C. Hetz, D. A. Hildeman, H. Ichijo, S. Inoue, M. Jäättelä, A. Janic, B. Joseph, P. J. Jost, T.-D. Kanneganti, M. Karin, H. Kashkar, T. Kaufmann, G. L. Kelly, O. Kepp, A. Kimchi, R. N. Kitsis, D. J. Klionsky, R. Kluck, D. V. Krysko, D. Kulms, S. Kumar, S. Lavandero, I. N. Lavrik, J. J. Lemasters, G. Liccardi, A. Linkermann, S. A. Lipton, R. A. Lockshin, C. López-Otín, T. Luedde, M. MacFarlane, F. Madeo, W. Malorni, G. Manic, R. Mantovani, S. Marchi, J.-C. Marine, S. J. Martin, J.-C. Martinou, P. G. Mastroberardino, J. P. Medema, P. Mehlen, P. Meier, G. Melino, S. Melino, E. A. Miao, U. M. Moll, C. Muñoz-Pinedo, D. J. Murphy, M. V. Niklison-Chirou, F. Novelli, G. Núñez, A. Oberst, D. Ofengeim, J. T. Opferman, M. Oren, M. Pagano, T. Panaretakis, M. Pasparakis, J. M. Penninger, F. Pentimalli, D. M. Pereira, S. Pervaiz, M. E. Peter, P. Pinton, G. Porta, J. H. M. Prehn, H. Puthalakath, G. A. Rabinovich, K. Rajalingam, K. S. Ravichandran, M. Rehm, J.-E. Ricci, R. Rizzuto, N. Robinson, C. M. P. Rodrigues, B. Rotblat, C. V. Rothlin, D. C. Rubinsztein, T. Rudel, A. Rufini, K. M. Ryan, K. A. Sarosiek, A. Sawa, E. Sayan, K. Schroder, L. Scorrano, F. Sesti, F. Shao, Y. Shi, G. S. Sica, J. Silke, H.-U. Simon, A. Sistigu, A. Stephanou, B. R. Stockwell, F. Strapazzon, A. Strasser, L. Sun, E. Sun, Q. Sun, G. Szabadkai, S. W. G. Tait, D. Tang, N. Tavernarakis, C. M. Troy, B. Turk, N. Urbano, P. Vandenabeele, T. Vanden Berghe, M. G. Vander Heiden, J. L. Vanderluit, A. Verkhratsky, A. Villunger, S. von Karstedt, A. K. Voss, K. H. Vousden, D. Vucic, D. Vuri, E. F. Wagner, H. Walczak, D. Wallach, R. Wang, Y. Wang, A. Weber, W. Wood, T. Yamazaki, H.-T. Yang, Z. Zakeri, J. E. Zawacka-Pankau, L. Zhang, H. Zhang, B. Zhivotovsky, W. Zhou, M. Piacentini, G. Kroemer, L. Galluzzi, Apoptotic cell death in disease—Current understanding of the NCCD 2023. *Cell Death Differ.* **30**, 1097–1154 (2023).
6. I. K. H. Poon, C. D. Lucas, A. G. Rossi, K. S. Ravichandran, Apoptotic cell clearance: Basic biology and therapeutic potential. *Nat. Rev. Immunol.* **14**, 166–180 (2014).
7. M. R. Elliott, K. S. Ravichandran, The dynamics of apoptotic cell clearance. *Dev. Cell* **38**, 147–160 (2016).
8. M. R. Elliott, F. B. Chekeni, P. C. Trampont, E. R. Lazarowski, A. Kadl, S. F. Walk, D. Park, R. I. Woodson, M. Ostankovich, P. Sharma, J. J. Lysiak, T. K. Harden, N. Leitinger, K. S. Ravichandran, Nucleotides released by apoptotic cells act as a find-me signal to promote phagocytic clearance. *Nature* **461**, 282–286 (2009).
9. F. B. Chekeni, M. R. Elliott, J. K. Sandilos, S. F. Walk, J. M. Kinchen, E. R. Lazarowski, A. J. Armstrong, S. Penuela, D. W. Laird, G. S. Salvesen, B. E. Isakson, D. A. Bayliss, K. S. Ravichandran, Pannexin 1 channels mediate "find-me" signal release and membrane permeability during apoptosis. *Nature* **467**, 863–867 (2010).
10. V. A. Fadok, D. R. Voelker, P. A. Campbell, J. J. Cohen, D. L. Bratton, P. M. Henson, Exposure of phosphatidylserine on the surface of apoptotic lymphocytes triggers specific recognition and removal by macrophages. *J. Immunol.* **148**, 2207–2216 (1992).
11. S. M. Pontejo, P. M. Murphy, Chemokines act as phosphatidylserine-bound "find-me" signals in apoptotic cell clearance. *PLOS Biol.* **19**, e3001259 (2021).
12. S. A. Freeman, S. Grinstein, Phagocytosis: Receptors, signal integration, and the cytoskeleton. *Immunol. Rev.* **262**, 193–215 (2014).
13. I. K. H. Poon, K. S. Ravichandran, Targeting efferocytosis in inflammaging. *Annu. Rev. Pharmacol. Toxicol.* **64**, 339–357 (2024).
14. E. Boada-Romero, J. Martinez, B. L. Heckmann, D. R. Green, The clearance of dead cells by efferocytosis. *Nat. Rev. Mol. Cell Biol.* **21**, 398–414 (2020).
15. V. Jaumouillé, C. M. Waterman, Physical constraints and forces involved in phagocytosis. *Front. Immunol.* **11**, 1097 (2020).

16. S. Mylvaganam, S. A. Freeman, S. Grinstein, The cytoskeleton in phagocytosis and macropinocytosis. *Curr. Biol.* **31**, R619–R632 (2021).
17. S. R. Barger, N. S. Reilly, M. S. Shutova, Q. Li, P. Maiuri, J. M. Heddleston, M. S. Mooseker, R. A. Flavell, T. Svitkina, P. W. Oakes, M. Krendel, N. C. Gauthier, Membrane-cytoskeletal crosstalk mediated by myosin-I regulates adhesion turnover during phagocytosis. *Nat. Commun.* **10**, 1249 (2019).
18. E. Hoijman, H.-M. Häkkinen, Q. Tolosa-Ramon, S. Jiménez-Delgado, C. Wyatt, M. Miret-Cuesta, M. Irimia, A. Callan-Jones, S. Wieser, V. Ruprecht, Cooperative epithelial phagocytosis enables error correction in the early embryo. *Nature* **590**, 618–623 (2021).
19. I. K. H. Poon, Y.-H. Chiu, A. J. Armstrong, J. M. Kinchen, I. J. Juncadella, D. A. Bayliss, K. S. Ravichandran, Unexpected link between an antibiotic, pannexin channels and apoptosis. *Nature* **507**, 329–334 (2014).
20. J. F. Kerr, Shrinkage necrosis: A distinct mode of cellular death. *J. Pathol.* **105**, 13–20 (1971).
21. R. Tixeira, T. K. Phan, S. Caruso, B. Shi, G. K. Atkin-Smith, C. Nedeva, J. D. Y. Chow, H. Puthalakath, M. D. Hulett, M. J. Herold, I. K. H. Poon, ROCK1 but not LIMK1 or PAK2 is a key regulator of apoptotic membrane blebbing and cell disassembly. *Cell Death Differ.* **27**, 102–116 (2020).
22. J. P. Santavanond, S. F. Rutter, G. K. Atkin-Smith, I. K. H. Poon, "Apoptotic bodies: Mechanism of formation, isolation and functional relevance," in *New Frontiers: Extracellular Vesicles*, S. Mathivanan, P. Fonseka, C. Nedeva, I. Atukorala, Eds., Subcellular Biochemistry (Springer International Publishing, 2021), pp. 61–88. https://doi.org/10.1007/978-3-030-67171-6_4.
23. M. Sebbagh, C. Renvoizé, J. Hamelin, N. Riché, J. Bertoglio, J. Bréard, Caspase-3-mediated cleavage of ROCK I induces MLC phosphorylation and apoptotic membrane blebbing. *Nat. Cell Biol.* **3**, 346–352 (2001).
24. M. L. Coleman, E. A. Sahai, M. Yeo, M. Bosch, A. Dewar, M. F. Olson, Membrane blebbing during apoptosis results from caspase-mediated activation of ROCK I. *Nat. Cell Biol.* **3**, 339–345 (2001).
25. K. A. Orlando, N. L. Stone, R. N. Pittman, Rho kinase regulates fragmentation and phagocytosis of apoptotic cells. *Exp. Cell Res.* **312**, 5–15 (2006).
26. G. K. Atkin-Smith, M. A. Miles, R. Tixeira, F. T. Lay, M. Duan, C. J. Hawkins, T. K. Phan, S. Paone, S. Mathivanan, M. D. Hulett, W. Chen, I. K. H. Poon, Plexin B2 is a regulator of monocyte apoptotic cell disassembly. *Cell Rep.* **29**, 1821–1831.e3 (2019).
27. G. Stasiłojć, S. Pinto, R. Wyszkowska, M. Wejda, E. M. Słomińska, M. Filipska, P. Koszałka, J. Świerczyński, J. E. O'Connor, J. J. Bigda, U937 variant cells as a model of apoptosis without cell disintegration. *Cell. Mol. Biol. Lett.* **18**, 249–262 (2013).
28. R. Tixeira, I. K. H. Poon, Disassembly of dying cells in diverse organisms. *Cell. Mol. Life Sci.* **76**, 245–257 (2019).
29. K. R. Mesa, P. Rompolas, G. Zito, P. Myung, T. Y. Sun, S. Brown, D. G. Gonzalez, K. B. Blagoev, A. M. Haberman, V. Greco, Niche-induced cell death and epithelial phagocytosis regulate hair follicle stem cell pool. *Nature* **522**, 94–97 (2015).
30. G. K. Atkin-Smith, S. Paone, D. J. Zanker, M. Duan, T. K. Phan, W. Chen, M. D. Hulett, I. K. H. Poon, Isolation of cell type-specific apoptotic bodies by fluorescence-activated cell sorting. *Sci. Rep.* **7**, 39846 (2017).
31. C. T. Mayer, A. Gazumyan, E. E. Kara, A. D. Gitlin, J. Golijanin, C. Viant, J. Pai, T. Y. Oliveira, Q. Wang, A. Escolano, M. Medina-Ramirez, R. W. Sanders, M. C. Nussenzweig, The microanatomic segregation of selection by apoptosis in the germinal center. *Science* **358**, eaao2602 (2017).
32. A. K. Grootveld, W. Kyaw, V. Panova, A. W. Y. Lau, E. Ashwin, G. Seuzaret, R. Dhenni, N. D. Bhattacharyya, W. H. Khoo, M. Biro, T. Mitra, M. Meyer-Hermann, P. Bertolino, M. Tanaka, D. A. Hume, P. I. Croucher, R. Brink, A. Nguyen, O. Bannard, T. G. Phan, Apoptotic cell fragments locally activate tingible body macrophages in the germinal center. *Cell* **186**, 1144–1161.e18 (2023).
33. Y. Zhu, S. C. Crowley, A. J. Latimer, G. M. Lewis, R. Nash, S. Kucenas, Migratory neural crest cells phagocytose dead cells in the developing nervous system. *Cell* **179**, 74–89.e10 (2019).
34. K. M. Ashby, K. A. Hogquist, A guide to thymic selection of T cells. *Nat. Rev. Immunol.* **24**, 103–117 (2024).
35. A. H. Wyllie, Glucocorticoid-induced thymocyte apoptosis is associated with endogenous endonuclease activation. *Nature* **284**, 555–556 (1980).
36. I. K. H. Poon, M. A. F. Parkes, L. Jiang, G. K. Atkin-Smith, R. Tixeira, C. D. Gregory, D. C. Ozkocak, S. F. Rutter, S. Caruso, J. P. Santavanond, S. Paone, B. Shi, A. L. Hodge, M. D. Hulett, J. D. Y. Chow, T. K. Phan, A. A. Baxter, Moving beyond size and phosphatidylserine exposure: Evidence for a diversity of apoptotic cell-derived extracellular vesicles in vitro. *J. Extracell. Vesicles* **8**, 1608786 (2019).
37. H.-J. Kim, E. S. Alonzo, G. Dorothee, J. W. Pollard, D. B. Sant'Angelo, Selective depletion of eosinophils or neutrophils in mice impacts the efficiency of apoptotic cell clearance in the thymus. *PLOS ONE* **5**, e11439 (2010).
38. J. N. Blau, A phagocytic function of hassall's corpuscles. *Nature* **208**, 564–567 (1965).
39. K. Köröskényi, G. Joós, Z. Szondy, Adenosine in the thymus. *Front. Pharmacol.* **8**, 932 (2017).
40. M. Kronlage, J. Song, L. Sorokin, K. Isfort, T. Schwerdtle, J. Leipziger, B. Robaye, P. B. Conley, H.-C. Kim, S. Sargin, P. Schön, A. Schwab, P. J. Hanley, Autocrine purinergic receptor signaling is essential for macrophage chemotaxis. *Sci. Signal.* **3**, ra55 (2010).
41. G. Joós, J. Jákim, B. Kiss, R. Szamosi, T. Papp, S. Felszeghy, T. Sághy, G. Nagy, Z. Szondy, Involvement of adenosine A3 receptors in the chemotactic navigation of macrophages towards apoptotic cells. *Immunol. Lett.* **183**, 62–72 (2017).
42. T. Iyoda, K. Nagata, M. Akashi, Y. Kobayashi, Neutrophils accelerate macrophage-mediated digestion of apoptotic cells in vivo as well as in vitro. *J. Immunol.* **175**, 3475–3483 (2005).
43. C. Odaka, T. Mizuochi, Macrophages are involved in DNA degradation of apoptotic cells in murine thymus after administration of hydrocortisone. *Cell Death Differ.* **9**, 104–112 (2002).
44. L. Julian, G. Naylor, G. R. Wickman, N. Rath, G. Castino, D. Stevenson, S. Bryson, J. Munro, L. McGarry, M. Mullin, A. Rice, A. Del Río Hernández, M. F. Olson, Defective apoptotic cell contractility provokes sterile inflammation, leading to liver damage and tumour suppression. *eLife* **10**, e61983 (2021).
45. K. Mardilovich, G. Naylor, L. Julian, N. Phinichkusolchit, K. Keeshan, K. Blyth, M. F. Olson, Caspase-resistant ROCK1 expression prolongs survival of Eμ-Myc B cell lymphoma mice. *Dis. Model. Mech.* **17**, dmm050631 (2024).
46. J. P. Santavanond, Y.-H. Chiu, R. Tixeira, Z. Liu, J. K. Y. Yap, K. W. Chen, C.-L. Li, Y.-R. Lu, J. Roncero-Carol, E. Hoijman, S. F. Rutter, B. Shi, G. F. Ryan, A. L. Hodge, S. Caruso, A. A. Baxter, D. C. Ozkocak, C. Johnson, Z. I. Day, A. J. Mayfosh, M. D. Hulett, T. K. Phan, G. K. Atkin-Smith, I. K. H. Poon, The small molecule raptinal can simultaneously induce apoptosis and inhibit PANX1 activity. *Cell Death Dis.* **15**, 123 (2024).
47. S. A. Hughes, M. Lin, A. Weir, B. Huang, L. Xiong, N. K. Chua, J. Pang, J. P. Santavanond, R. Tixeira, M. Doerflinger, Y. Deng, C.-H. Yu, N. Silke, S. A. Conos, D. Frank, D. S. Simpson, J. M. Murphy, K. E. Lawlor, J. S. Pearson, J. Silke, M. Pellegrini, M. J. Herold, I. K. H. Poon, S. L. Masters, M. Li, Q. Tang, Y. Zhang, M. Rashidi, L. Geng, J. E. Vince, Caspase-8-driven apoptotic and pyroptotic crosstalk causes cell death and IL-1β release in X-linked inhibitor of apoptosis (XIAP) deficiency. *EMBO J.* **42**, e110468 (2023).
48. G. Anderson, W. E. Jenkinson, T. Jones, S. M. Parnell, F. A. M. Kinsella, A. J. White, J. E. Pongrac'z, S. W. Rossi, E. J. Jenkinson, Establishment and functioning of intrathymic microenvironments. *Immunol. Rev.* **209**, 10–27 (2006).
49. E. Uchimura, N. Watanabe, O. Niwa, M. Muto, Y. Kobayashi, Transient infiltration of neutrophils into the thymus in association with apoptosis induced by whole-body X-irradiation. *J. Leukoc. Biol.* **67**, 780–784 (2000).
50. V. Ruprecht, S. Wieser, A. Callan-Jones, M. Smutny, H. Morita, K. Sako, V. Barone, M. Ritsch-Marte, M. Sixt, R. Voituriez, C.-P. Heisenberg, Cortical contractility triggers a stochastic switch to fast amoeboid cell motility. *Cell* **160**, 673–685 (2015).
51. H. De Belly, A. Stubb, A. Yanagida, C. Labouesse, P. H. Jones, E. K. Paluch, K. J. Chalut, Membrane tension gates ERK-mediated regulation of pluripotent cell fate. *Cell Stem Cell* **28**, 273–284.e6 (2021).
52. S. J. Heasman, A. J. Ridley, Mammalian Rho GTPases: New insights into their functions from in vivo studies. *Nat. Rev. Mol. Cell Biol.* **9**, 690–701 (2008).
53. D. Vorselen, S. R. Barger, Y. Wang, W. Cai, J. A. Theriot, N. C. Gauthier, M. Krendel, Phagocytic "teeth" and myosin-II "jaw" power target constriction during phagocytosis. *eLife* **10**, e68627 (2021).
54. S. Heimer, G. Knoll, K. Schulze-Osthoff, M. Ehrenschwender, Raptinal bypasses BAX, BAK, and BOK for mitochondrial outer membrane permeabilization and intrinsic apoptosis. *Cell Death Dis.* **10**, 556 (2019).
55. R. Palchaudhuri, M. J. Lambrecht, R. C. Botham, K. C. Partlow, T. J. Van Ham, K. S. Putt, L. T. Nguyen, S.-H. Kim, R. T. Peterson, T. M. Fan, P. J. Hergenrother, A small molecule that induces intrinsic pathway apoptosis with unparalleled speed. *Cell Rep.* **13**, 2027–2036 (2015).
56. T. Le, I. Ferling, L. Qiu, C. Nabaile, L. Assunção, C. D. Roskelley, S. Grinstein, S. A. Freeman, Redistribution of the glycocalyx exposes phagocytic determinants on apoptotic cells. *Dev. Cell* **59**, 853–868.e7 (2024).
57. M. V. Baranov, M. Kumar, S. Sacanna, S. Thutupalli, G. van den Bogaart, Modulation of immune responses by particle size and shape. *Front. Immunol.* **11**, 607945 (2020).
58. J. A. Champion, S. Mitragotri, Role of target geometry in phagocytosis. *Proc. Natl. Acad. Sci. U.S.A.* **103**, 4930–4934 (2006).
59. D. M. Richards, R. G. Endres, Target shape dependence in a simple model of receptor-mediated endocytosis and phagocytosis. *Proc. Natl. Acad. Sci. U.S.A.* **113**, 6113–6118 (2016).
60. O. Campàs, I. Noordstra, A. S. Yap, Adherens junctions as molecular regulators of emergent tissue mechanics. *Nat. Rev. Mol. Cell Biol.* **25**, 252–269 (2024).
61. M. Hamieh, A. Dobrin, A. Cabriolu, S. J. C. van der Stegen, T. Giavridis, J. Mansilla-Soto, J. Eyquem, Z. Zhao, B. M. Whitlock, M. M. Miele, Z. Li, K. M. Cunanan, M. Huse, R. C. Hendrickson, X. Wang, I. Rivière, M. Sadelain, CAR T cell trogocytosis and cooperative killing regulate tumour antigen escape. *Nature* **568**, 112–116 (2019).
62. P. Schriek, A. C. Ching, N. S. Moily, J. Moffat, L. Beattie, T. M. Steiner, L. M. Hosking, J. M. Thurman, V. M. Holers, S. Ishido, M. H. Lahoud, I. Caminschi, W. R. Heath, J. D. Mintern,

J. A. Villadangos, Marginal zone B cells acquire dendritic cell functions by trogocytosis. *Science* **375**, eabf7470 (2022).
63. D. Vorselen, Y. Wang, M. M. de Jesus, P. K. Shah, M. J. Footer, M. Huse, W. Cai, J. A. Theriot, Microparticle traction force microscopy reveals subcellular force exertion patterns in immune cell-target interactions. *Nat. Commun.* **11**, 20 (2020).
64. A. De Lozanne, J. A. Spudich, Disruption of the *Dictyostelium* myosin heavy chain gene by homologous recombination. *Science* **236**, 1086–1091 (1987).
65. K. Murthy, P. Wadsworth, Myosin-II-dependent localization and dynamics of F-actin during cytokinesis. *Curr. Biol.* **15**, 724–731 (2005).
66. A. C. Doran, A. Yurdagul Jr., I. Tabas, Efferocytosis in health and disease. *Nat. Rev. Immunol.* **20**, 254–267 (2020).
67. H. Wang, H. Yang, C. S. Shivalila, M. M. Dawlaty, A. W. Cheng, F. Zhang, R. Jaenisch, One-step generation of mice carrying mutations in multiple genes by CRISPR/Cas-mediated genome engineering. *Cell* **153**, 910–918 (2013).
68. A. I. Kousa, L. Jahn, K. Zhao, A. E. Flores, D. Acenas II, E. Lederer, K. V. Argyropoulos, A. L. Lemarquis, D. Granadier, K. Cooper, M. D'Andrea, J. M. Sheridan, J. Tsai, L. Sikkema, A. Lazrak, K. Nichols, N. Lee, R. Ghale, F. Malard, H. Andrlova, E. Velardi, S. Youssef, M. Burgos da Silva, M. Docampo, R. Sharma, L. Mazutis, V. C. Wimmer, K. L. Rogers, S. DeWolf, B. Gipson, A. L. C. Gomes, M. Setty, D. Pe'er, L. Hale, N. R. Manley, D. H. D. Gray, M. R. M. van den Brink, J. A. Dudakov, Age-related epithelial defects limit thymic function and regeneration. *Nat. Immunol.* **25**, 1593–1606 (2024).
69. M. Behrndt, G. Salbreux, P. Campinho, R. Hauschild, F. Oswald, J. Roensch, S. W. Grill, C.-P. Heisenberg, Forces driving epithelial spreading in zebrafish gastrulation. *Science* **338**, 257–260 (2012).
70. J.-L. Maître, H. Berthoumieux, S. F. G. Krens, G. Salbreux, F. Jülicher, E. Paluch, C.-P. Heisenberg, Adhesion functions in cell sorting by mechanically coupling the cortices of adhering cells. *Science* **338**, 253–256 (2012).
71. M. Kajita, C. Hogan, A. R. Harris, S. Dupre-Crochet, N. Itasaki, K. Kawakami, G. Charras, M. Tada, Y. Fujita, Interaction with surrounding normal epithelial cells influences signalling pathways and behaviour of Src-transformed cells. *J. Cell Sci.* **123**, 171–180 (2010).
72. C. B. Kimmel, W. W. Ballard, S. R. Kimmel, B. Ullmann, T. F. Schilling, Stages of embryonic development of the zebrafish. *Dev. Dyn.* **203**, 253–310 (1995).

Acknowledgments: We would like to thank the La Trobe University Bioimaging Platform, La Trobe Animal Research and Teaching Facility, and Walter and Eliza Hall Institute histology team for technical support. We also thank the bioimaging platform and fish facility from IDIBELL, the help of P-CMRC members, H. Hakkinen for assistance with the zebrafish imaging, V. Ruprecht for sharing zebrafish lines and resources, and the CRG for supporting the initial zebrafish experiments. The generation of PANX1^{nc} mice used in this study was supported by Phenomics Australia and the Australian Government through the National Collaborative Research Infrastructure Strategy (NCRIS) program. Schemes shown on Figs. 3 and 5 and fig. S6 were prepared using BioRender software. **Funding:** This work was supported by National Health and Medical Research Council (GNT1173662 to I.K.H.P., 2009287 to G.K.A-S., and 2029937 to D.H.D.G.), Australia Research Council (DP200100458 to I.K.H.P.), Ministry of Science and Innovation of Spain (PID2020-117540GB-I00 to E.H.), AGAUR (2022-SGR-00974 to E.H.), Canadian Institutes of Health (PJT-169106 to M.F.O.), Canada Research Chair program (950-231665 to M.F.O.), Serra-Hunter program from the Government of Catalunya (to E.H.), and FPU 22/04307 and FI 100057 (J.R.-C.).
Author contributions: Conceptualization: I.K.H.P. and E.H. Experimental design: J.P.S., G.K.A.-S., G.F.R., I.K.H.P., and E.H. with inputs from I.L.-G., J.R.-C., L.J., A.L.H., D.C.O., K.Z., M.D.H., A.A.B., J.P.S., G.K.A.-S. Investigation: D.C.O. (TEM experiments); K.Z. (assistance with tissue clearing); D.H.D.G. (supervision); M.F.O. (generation of ROCK1^{nc} mice); M.J.H., A.J.K., G.F.R., and R.T. (generation of PANX1^{nc} mice); E.H., I.L.-G., and J.R-C. (zebrafish experiments); J.P.S. (all other experiments). Writing: I.K.H.P. and E.H. Figures assembly: J.P.S., G.K.A.-S., I.K.H.P., E.H., I.L.-G., J.R-C., A.L.H., and D.C.O. **Competing interests:** The authors declare that they have no competing interests.
Data and materials availability: All data and code needed to evaluate and reproduce the results in the paper are present in the paper and/or the Supplementary Materials.

Submitted 6 June 2025
Accepted 14 November 2025
Published 17 December 2025
10.1126/sciadv.adz5264